Modelling tunnelling-induced deformation in stiff soils with a hyperelastic-plastic anisotropic model

Marcin Cudny*, Katarzyna Lisewska

Gdańsk University of Technology, Faculty of Civil and Environmental Engineering, ul. Narutowicza 11/12, 80-233 Gdańsk, Poland

Manuel Winkler, Thomas Marcher

Graz University of Technology, Institute of Rock Mechanics and Tunnelling, Rechbauerstraße 12, A-8010 Graz, Austria

Abstract

In this paper, the tunnelling-induced deformation in anisotropic stiff soils is analysed using FE modelling. The influence of material description is investigated rather than an advanced simulation of the tunnelling method. A new hyperelastic-plastic model is proposed to describe the anisotropic mechanical behaviour of stiff highly overconsolidated soil. This model can reproduce the superposition of variable stress-induced anisotropy and constant inherent cross-anisotropy of the small strain stiffness. Additionally, a BRICK-type framework accounts for the strain degradation of stiffness. Formulation of the novel model is presented. The tunnelling-induced deformation is first investigated in plane strain conditions for a simple boundary value problem of homogeneous ground. The influence of initial stress anisotropy and inherent cross-anisotropy is inspected. Later, the results of 2D simulations are compared with the analogous results of 3D simulations considering different excavated length of the tunnel sections. The tunnelling process is reproduced by introduction of a supported excavation and a lining contraction stage in undrained conditions. Finally, the tunnelling case study at St James Park is back analysed using the proposed material model in plane strain conditions. The obtained calculation results are compared with the field measurements and discussed.

Keywords: cross-anisotropy, hyperelastic-plastic model, small strain stiffness anisotropy, stiff soils, tunnelling-induced deformation

---

*Corresponding author.
tel: +48 607 756 675
Email addresses:* mcud@pg.edu.pl (Marcin Cudny), katkowa3@pg.edu.pl (Katarzyna Lisewska), winkler@tugraz.at (Manuel Winkler), thomas.marcher@tugraz.at (Thomas Marcher)

List of symbols

c	Effective cohesion
$\mathbf{C}, C_{ijkl}$	Fourth-order elastic compliance tensor
$\text{diag}(a_1, ..., a_n)$	Diagonal matrix constructed from vector $\mathbf{a}$
$\mathbf{e}, e_{ij}$	Deviatoric part of the strain tensor,
	$e_{ij} = \varepsilon_{ij} - \frac{1}{3}\varepsilon_{kk}\,\delta_{ij}$
E	Young's modulus
G	Shear modulus
K	Stress ratio,
	$K = \sigma_h/\sigma_v$ or $K = \sigma_{xx}/\sigma_{yy}$
m	Order of stiffness dependency on stress (exponent in the power law)
$\mathbf{M}, M_{ij}$	Microstructure tensor
p	Mean effective stress,
	$p = -\frac{1}{3}\sigma_{kk}$
q	Deviatoric stress,
	$q = \sqrt{\frac{3}{2}s_{ij}s_{ij}}$
$\mathbf{s}, s_{ij}$	Deviatoric part of the stress tensor,
	$s_{ij} = \sigma_{ij} + p\,\delta_{ij}$
u_x, u_y, u_z	Displacement components in x, y, z directions, respectively
$\mathbf{v}, v_i$	Symmetry axis in a cross-anisotropic material (unit vector)
W	Elastic potential
x_i	Geometrical axes (in 2D calculations x_2 or y is vertical,
	in 3D calculations x_3 or z is vertical)
α_G	Small strain stiffness cross-anisotropy coefficient,
	$\alpha_G = G_{0hh}/G_{0vh}$
β	Parameter coupling the Poisson's ratio and the order of stress dependency
	of the elastic stiffness in Vermeer's model
$\boldsymbol{\delta}, \delta_{ij}$	Kronecker's symbol
$\boldsymbol{\varepsilon}, \varepsilon_{ij}$	Strain tensor, compression negative

ϕ	Effective friction angle
ν	Poisson's ratio
$\boldsymbol{\sigma}, \sigma_{ij}$	Effective Cauchy stress tensor, compression negative
$\sigma_1, \sigma_2, \sigma_3$	Major, intermediate and minor principal stress components, respectively
$()_0, ()^0$	Initial or small strain values
$()_{\mathrm{ref}}, ()^{\mathrm{ref}}$	Reference values
$()_{\mathrm{s}}, ()_{\mathrm{t}}$	Secant and tangent parameters or operators, respectively
$()_{\mathrm{u}}$	Undrained parameter
$()_v, ()_h$	Cross-anisotropic components along the symmetry axis and in the plane of isotropy, respectively (here collinear with vertical and horizontal direction)
$\overline{()}$	Functions of both stress and jointed stress-microstructure invariants
$\cdot$	Single contraction, e.g. $\mathbf{a} \cdot \mathbf{b} = a_i b_i \ \text{or} \ \mathbf{A} \cdot \mathbf{b} = A_{ij} b_j$
$\otimes$	Dyadic or outer product, e.g. $\mathbf{A} = \mathbf{a} \otimes \mathbf{b} = a_i b_j = A_{ij}$
$\| \ \|$	Euclidean norm, e.g. $\|\mathbf{x}\| = \sqrt{x_i x_i} \ \text{or} \ \|\boldsymbol{\varepsilon}\| = \sqrt{\varepsilon_{ij} \varepsilon_{ij}}$
$\mathrm{tr}\,()$	Trace of a tensor, e.g. $\mathrm{tr}\,\boldsymbol{\sigma} = \sigma_{ii}$
$()^n$	Power of a tensor, e.g. $\boldsymbol{\sigma}^n = \overbrace{\boldsymbol{\sigma} \cdot \boldsymbol{\sigma} \cdot \ldots \cdot \boldsymbol{\sigma}}^{n} \ \text{or} \ \mathrm{tr}\,\boldsymbol{\sigma}^2 = \mathrm{tr}\,(\sigma_{ij}\sigma_{jk}) = \sigma_{ij}\sigma_{ij}$

1. Introduction

In geotechnics, tunnelling problems are usually related to the unloading and resulting strong redistribution of stress within the subsoil. The principal stress directions undergo large rotations and the ratios of principal stress components change significantly in the vicinity of tunnel excavation. Soils with anisotropic microstructure show directional dependent material properties and the stress redistribution occurs relatively to the material directions. This causes significant changes of the stiffness during tunnelling, see Fig. 1. The numerical modelling of the
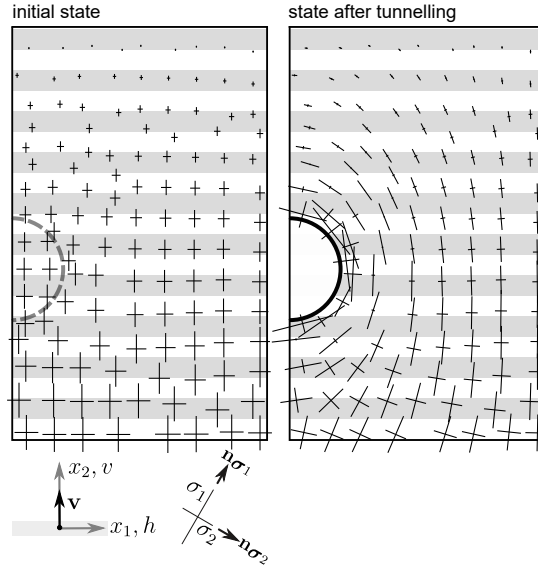
3

Figure 1: Changes of principal stress components σ_i and directions $\mathbf{n}_{\boldsymbol{\sigma}i}$ due to tunnelling. A cross-anisotropic soil is considered and the geometrical axes (x_1, x_2) are collinear with the material directions. They represent the plane of symmetry (h) and the axis of symmetry $(\mathbf{v}, v)$, respectively. This standard configuration is prescribed in the numerical analyses presented in the article.

geotechnical boundary value problems (BVP) involving unloading phases requires an appropriate material description of the soil behaviour. It should allow an accurate simulation of the mechanical characteristics in the range of small and intermediate strains. This is particularly relevant in the stiff overconsolidated fine-grained soils. The most important are the pre-failure stiffness nonlinearity related to the barotropy, the strain degradation of the current tangent stiffness moduli and the stiffness anisotropy. In the numerical analyses of tunnelling-induced deformation with the soil models based on the linear isotropic elasticity for the small strain stiffness, the calculated displacements are shown to be too small when compared with the field measurements, judging by e.g. the depth and steepness of the greenfield surface settlement troughs [1]. The incorporation of the stiffness nonlinearity in the soil model is an important improvement [16]. However, the stiffness anisotropy should be additionally taken into account because it results in better accuracy of the estimated deformation [23, 1, 29, 12, 33, 3, 21].

Constitutive models implemented in the commercial codes for geotechnical simulations rarely allow to simulate both the nonlinear and anisotropic pre-failure stiffness of soils. It is usually related to a more complicated formulation and implementation than in the case of isotropic models. The use of anisotropic models is also uncommon in practice due to the

4

scarcity of additional parameters describing the anisotropy and the lack of standardisation in determining them. However, the recent improvement of measurement tools in experimental soil mechanics enables the design and execution of precise investigations of the stiffness anisotropy. Usually the cross-anisotropic shear moduli are measured in the triaxial apparatus equipped with seismic bender elements oriented both vertically and horizontally. Performance of the anisotropic models is typically validated in element tests. However, the most challenging is the final application of the developed model in the real BVPs where the complexity is not only related to the material description but also to the modelling of drainage conditions, groundwater flow, consolidation and heterogeneous geological structure. The robustness and simplicity of an anisotropic constitutive model are highly desired.

The description of anisotropy in the proposed model is included entirely in the hyperelastic small strain kernel. The hyperelastic stress-strain relation is derived from the stress and microstructure-based potential function and it allows to model both the stress-induced anisotropy, related to the actual stress obliquity, and constant inherent cross-anisotropy defined by material directions. The crucial cross-anisotropic parameter is the coefficient α_G being the ratio of the shear modulus in the plane of symmetry G_{0hh} to the shear modulus in the plane passing through the axis of symmetry G_{0vh}. The remaining elements of the proposed model are isotropic. These elements are the stiffness degradation procedure based on the BRICK-type model [36] and the shear strength criterion by Matsuoka-Nakai [25]. However, the anisotropic stiffness from the small strain hyperelastic kernel is spread to the intermediate and large strains and influences the deformation and the stress paths in undrained conditions [39, 46, 30]. A simplicity of the model is due to the lack of closed conventional yield surfaces in the stress space and the assumption that the inherent cross-anisotropy is constant in stiff soils. This does not allow simulation of the evolution of anisotropy for large strains, e.g. during the initial geological history of the deposit [27, 2]. Hence, the initial K_0 stress ratio needs to be specified before the simulations.

In the first part of the FE simulations presented in the article, a parametric study of the influence of the initial K_0 stress conditions and the coefficient of inherent cross-anisotropy α_G on the induced deformation is performed in a simple tunnelling BVP. Next, the model efficiency is examined in the back analysis of the well-known case study of the twin-tunnel construction beneath St James's Park in London [32].

2. Hyperelastic-plastic material model

The preliminary version of the used constitutive description was formulated in [7]. Verification of the model in some exemplary boundary value problems (BVP) of tunnelling and excavation is given in [8]. The model is based on the anisotropic hyperelastic kernel. The reference tangent shear modulus is subjected to the strain degradation. The stress states are limited by the isotropic shear strength criterion proposed by Matsuoka and Nakai [25].

2.1. Small strain anisotropic hyperelastic kernel

The novel hyperelastic model has been thoroughly described in [9]. It is a modification of the Vermeer's hyperelastic model [43] with incorporation of the inherent cross-anisotropy. In the original hyperelastic formulation, the elastic potential is a function of the following stress invariant:

$$Q(\boldsymbol{\sigma}) = \frac{1}{2}\mathrm{tr}\,\boldsymbol{\sigma}^2 = \frac{1}{2}\sigma_{ij}\sigma_{ij}, \tag{1}$$

which provides the stress-induced anisotropy of the resulting hyperelastic stiffness. In the modified model, the inherent anisotropy is additionally taken into account using the joint stress–microstructure invariant Q_M defined as:

$$Q_M(\boldsymbol{\sigma}, \mathbf{M}) = \frac{1}{2}\mathrm{tr}\,(\boldsymbol{\sigma}^2 \cdot \mathbf{M}) = \frac{1}{2}\,M_{ij}\sigma_{jk}\sigma_{ki}, \tag{2}$$

where $\mathbf{M}$ is the second-order microstructure tensor [4]. In the case of cross-anisotropy, $\mathbf{M}$ is calculated as the following dyadic product:

$$\mathbf{M} = \mathbf{v} \otimes \mathbf{v} \quad \text{or} \quad M_{ij} = v_i v_j, \tag{3}$$

where the unit vector $\mathbf{v}$ defines the symmetry axis normal to the plane of isotropy. Here, the horizontal plane of isotropy with the vertical symmetry axis is assumed, i.e. $\mathbf{v} = [0, 1, 0]^T$ and $\mathbf{M} = \mathrm{diag}(0, 1, 0)$, see Fig. 1. The invariants Q and Q_M are grouped to obtain the following mixed invariant:

$$\overline{Q}(\boldsymbol{\sigma}, \mathbf{M}) = c_1 Q(\boldsymbol{\sigma}) + c_2 Q_M(\boldsymbol{\sigma}, \mathbf{M}) = \frac{1}{2}\overbrace{(c_1\delta_{ij} + c_2 M_{ij})}^{m_{ij}}\sigma_{jk}\sigma_{ki} = \frac{1}{2}m_{ij}\sigma_{jk}\sigma_{ki}, \tag{4}$$

6

where c_1 and c_2 are the material constants. They account for the stress-induced and inherent cross-anisotropy. The stress-induced anisotropy may vary with stress, but the inherent cross-anisotropy is constant in the model.

The anisotropic elastic potential in the modified formulation is defined as:

$$\overline{W}(\boldsymbol{\sigma}, \mathbf{M}) = \frac{3 p_{\text{ref}}^{1-\beta}}{2\, G_0^{\text{ref}}(1+\beta)} \left[\frac{2}{3} \overline{Q}(\boldsymbol{\sigma}, \mathbf{M}) \right]^{(1+\beta)/2}, \tag{5}$$

where G_0^{ref} is the reference shear modulus. It is measured at the isotropic stress $p = p_{\text{ref}}$. The potential represents the negative Gibbs free energy which is a function of stress of order $1 + \beta$. In Eq. 5, β is a material parameter that controls the order of stiffness stress dependency, $m = 1 - \beta$, and the cross-anisotropic Poisson's ratios [9]. The second stress derivative of $\overline{W}(\boldsymbol{\sigma}, \mathbf{M})$ returns the tangent compliance $\mathbf{C}^{\text{t}}(\boldsymbol{\sigma}, \mathbf{M})$ of the anisotropic hyperelastic material:

$$C_{ijkl}^{\text{t}} = \frac{\partial^2 \overline{W}(\boldsymbol{\sigma}, \mathbf{M})}{\partial \sigma_{ij} \partial \sigma_{kl}} = \frac{p_{\text{ref}}^{1-\beta}}{4\, G_0^{\text{ref}}} \left[\frac{2}{3} \overline{Q}(\boldsymbol{\sigma}, \mathbf{M}) \right]^{(\beta-1)/2} A_{ijkl}, \tag{6}$$

where

$$A_{ijkl} = (\delta_{jl} m_{ik} + \delta_{il} m_{jk})^{\text{symm}} - (1-\beta) \frac{(\sigma_{al} m_{ak} + \sigma_{bk} m_{bl})(\sigma_{aj} m_{ai} + \sigma_{bi} m_{bj})}{4\, \overline{Q}(\boldsymbol{\sigma}, \mathbf{M})}, \tag{7}$$

and

$$(\delta_{jl} m_{ik} + \delta_{il} m_{jk})^{\text{symm}} = \frac{1}{2}(\delta_{jl} m_{ik} + \delta_{jk} m_{il} + \delta_{il} m_{jk} + \delta_{ik} m_{jl}). \tag{8}$$

In the implementation, the fourth-order compliance tensor is transformed into the Voigt matrix notation and inverted either analytically or numerically (in a general 3D case with an arbitrary orientation of the plane of isotropy) to obtain the tangent stiffness matrix.

The parameters proposed in the original formulation are: $G_0^{\text{ref}}, c_1, c_2, \beta, p_{\text{ref}}$. However, it is convenient to use the cross-anisotropic small strain stiffness parameters measured in the laboratory or reported in the literature, e.g.: E_{0v}, E_{0h} - Young's moduli in the vertical and horizontal direction, respectively; G_{0vh}, G_{0hh} - Shear moduli in the vertical plane and in the plane of isotropy, respectively; ν_{0vh} - Poisson's ratio for horizontal strain due to vertical strain; ν_{0hh} - Poisson's ratio for horizontal strain due to complementary horizontal strain. Typical values of these parameters for fine-grained soils, obtained within a specific range of stress, are
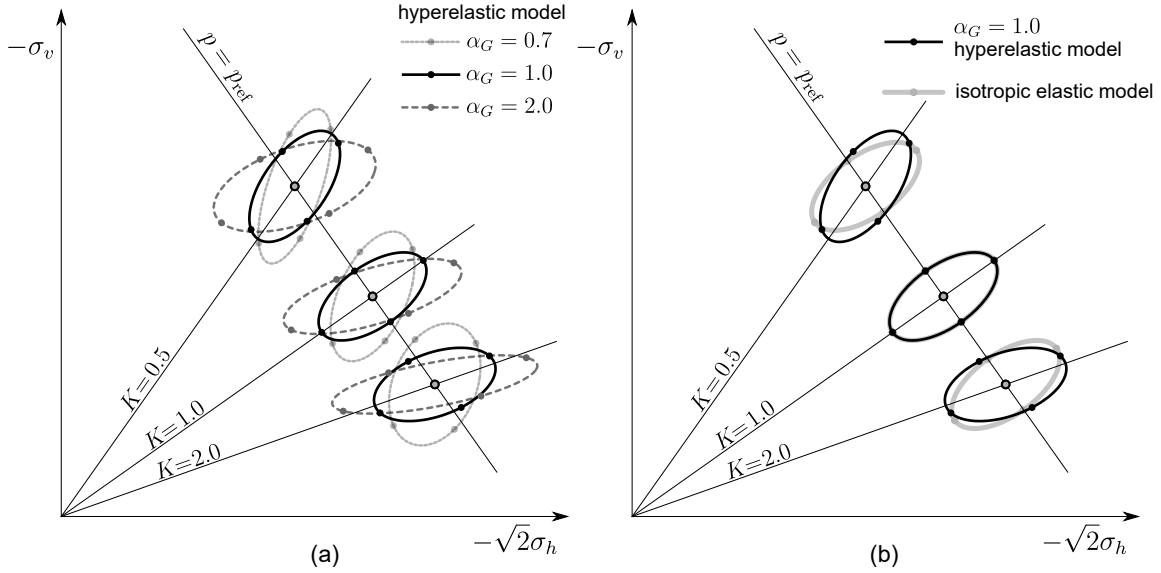
Figure 2: Response envelopes of the initial hyperelastic stiffness plotted for different values of the axisymmetric stress ratio ($K = 0.5, 1.0, 2.0$) and the inherent cross-anisotropy coefficient ($\alpha_G = 0.7, 1.0, 2.0$). Combinations of these conditions are applied in the exemplary FE tunnelling simulations presented in Sect. 3.

reported in [26, 7]. It is shown in [9] that by fixing $c_1 = 1.0$, the constant c_2 is directly related to the inherent cross-anisotropy coefficient α_G:

$$c_2 = 2(\alpha_G - 1), \quad \text{with} \quad \alpha_G = \frac{G_{0hh}}{G_{0vh}}, \tag{9}$$

The simplified parameter set is: $G_{0vh}^{\text{ref}}, \alpha_G, \beta, p_{\text{ref}}$. Therefore, the *isotropic* reference shear modulus G_0^{ref} in Eq. 5 or Eq. 6 should be calculated from:

$$G_0^{\text{ref}}(G_{0vh}^{\text{ref}}, \alpha_G, \beta) = G_{0vh}^{\text{ref}} \alpha_G \left(\sqrt{\frac{1 + 2\alpha_G}{3}} \right)^{\beta - 1}. \tag{10}$$

Remaining relations between cross-anisotropic Young's moduli, Poisson's ratios and the parameters of the simplified set are given in [9].

The directional distribution of the stiffness in the presented hyperelastic model may be illustrated using response envelopes [17]. A response envelope is a polar diagram of the tangent stiffness or compliance tensor. Response envelopes for tangent stiffness are usually shown in the axisymmetric stress plane ($\sqrt{2}\sigma_h - \sigma_v$) as a closed curve representing the stiffness response to a circular strain probe. This is shown in Fig. 2 for $G_{0vh}^{\text{ref}} = \text{const}$, $\beta = 0.5$ and different values of the inherent cross-anisotropy coefficient α_G and the axisymmetric stress ratio K. Solely the
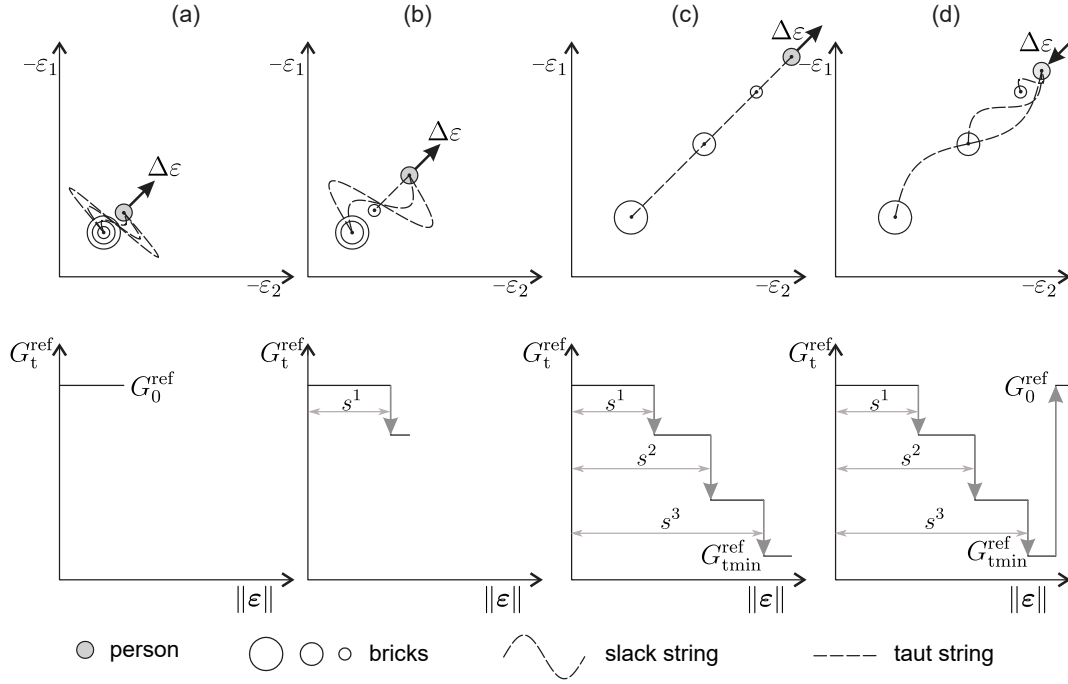
8

Figure 3: Strain degradation of stiffness in the Brick-type model presented for an exemplary monotonic strain path (a-c) followed by sharp unloading (d). A person is pulling $N_{\mathrm{b}} = 3$ bricks which when moved give stepwise drops of the reference tangent shear modulus $G_{\mathrm{t}}^{\mathrm{ref}}$ from G_0^{ref} down to $G_{\mathrm{tmin}}^{\mathrm{ref}}$. Proportions of the stiffness drops can be defined for each brick separately.

value of G_{0vh}^{ref} scales the size of response envelopes, and it is selected for the optimum visual effect. The influence of pure inherent cross-anisotropy on the directional distribution of stiffness is shown for the isotropic stress ratio $K = 1.0$ and $\alpha_G = 0.7, 2.0$. In Fig. 2b, the influence of pure stress-induced anisotropy is presented for $K = 0.5, 2.0$ and $\alpha_G = 1.0$. Response envelopes for the isotropic elastic model ($E_0 = 2G_{0vh}(1 + \nu_0)$, $\nu_0 = 0.2$) serve as comparison. The mixed stress-induced and inherent anisotropy for $K \neq 1.0$ and $\alpha_G \neq 1.0$ are illustrated in Fig. 2a.

2.2. Strain degradation of stiffness

The pre-failure behaviour concerning the gradual strain degradation of the stiffness is simulated with the Brick-type model based on the original formulation by Simpson [37]. The Brick model may be classified as an example of the concept of nested yield surfaces defined in the strain space [28, 34]. It allows to simulate the stiffness degradation during monotonic loading and the recovery of high initial stiffness after sharp strain path reversals. Different versions of the Brick-type model are reported in the literature giving satisfactory results in various FE computations, e.g. [38, 22, 24, 6, 11, 45, 21]. The Brick algorithm used in the calculations

9

presented in this paper is described in detail in [10].

The idea of the model is presented schematically in Fig. 3. It uses the analogy of a man pulling the finite number of bricks on strings. Initially, strings of different lengths s^j are slack (Fig. 3a) and the current tangent reference shear modulus G_t^{ref} is equal to the initial value G_0^{ref} obtained from Eq. 10. When the man moves, the strings become taut one by one, pulling the next brick. The man's movement represents strain and the strings lengths are radii of the nested circular yield surfaces in the strain space. Each time the next brick starts being pulled by the man, the tangent modulus G_t^{ref} is degraded in steps (Fig. 3b). When all bricks are pulled (Fig. 3c), the reference shear modulus achieves the constant minimum value $G_{\text{tmin}}^{\text{ref}}$. It should be noted that $G_{\text{tmin}}^{\text{ref}}$ is the internal *isotropic* stiffness constant and for $\alpha_G \neq 1.0$ its value, similarly like G_0^{ref}, should be calculated from Eq. 10 using $G_{vh\text{min}}^{\text{ref}}$. In the analogous BRICK formulation presented in [10] the minimum value of the reference shear modulus is denoted as $G_{\text{ur}}^{\text{ref}}$ and it describes the unloading-reloading stiffness. When the loading direction in the strain space changes, the strings are loosen and the high initial modulus G_0^{ref} is recovered (Fig. 3d).

In [10], coordinates of the man and bricks are defined in the general 6-dimensional strain space; however, the relative strain distances between the man and bricks are measured by the
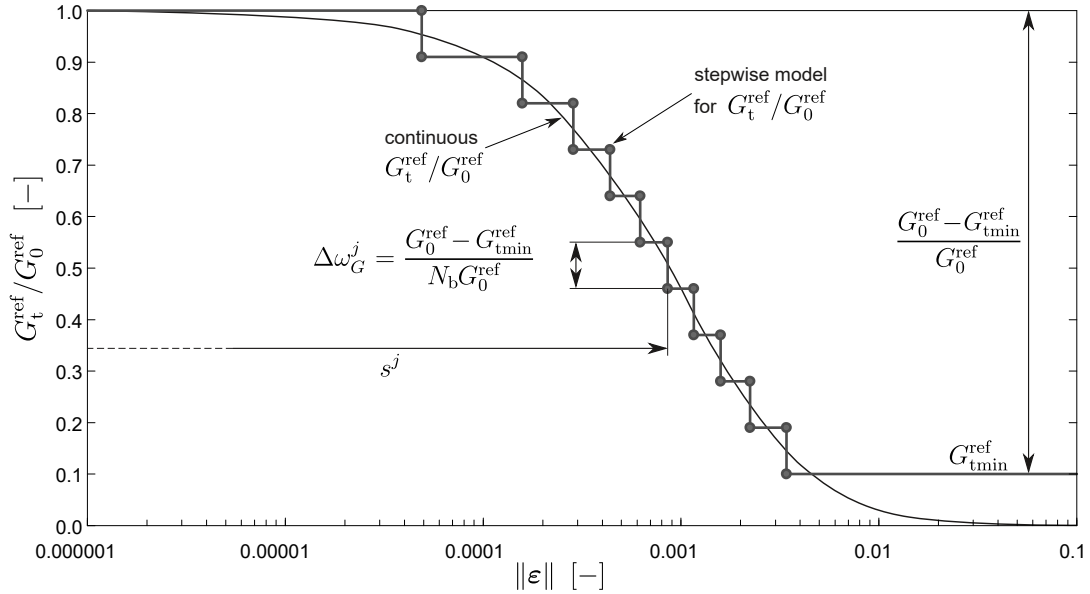

Figure 4: The stepwise representation of the S-shaped curve to model strain degradation of the reference tangent shear modulus G_t^{ref} in the BRICK-type model. The Euclidian norm of strain $\|\varepsilon\|$ is used as a measure of the distance between the man and bricks. $N_\text{b} = 10$ bricks are employed with equal stiffness proportions ($\Delta\omega_G^j = \Delta\omega_G = \text{const}$).

10

shear strain invariant $\gamma = \sqrt{3/2}\,\|\mathbf{e}\|$. Here, a modified solution is employed, and the relative strain distance is measured by the Euclidian norm of strain $\|\boldsymbol{\varepsilon}\|$. Parameters of the used BRICK model describe the stepwise representation of the S-shaped curve shown in Fig. 4. The S-shape curve presents the degradation of the stiffness ratio $G_{\mathrm{t}}^{\mathrm{ref}}/G_0^{\mathrm{ref}}$ with increasing strain measured as $\|\boldsymbol{\varepsilon}\|$. The stepwise S-shaped curve approximates the following continuous model:

$$\frac{G_{\mathrm{t}}^{\mathrm{ref}}}{G_0^{\mathrm{ref}}} = \left(\frac{\|\boldsymbol{\varepsilon}\|_{\mathrm{sh}}}{\|\boldsymbol{\varepsilon}\|_{\mathrm{sh}} + \frac{3}{7}\|\boldsymbol{\varepsilon}\|}\right)^2, \tag{11}$$

where $\|\boldsymbol{\varepsilon}\|_{\mathrm{sh}}$ is the shape parameter controlling the steepness of the S-shaped curve. Equation 11 is a modified version of the proposal for degradation of $G_{\mathrm{t}}^{\mathrm{ref}}$ with shear strain by Santos and Correia [35]. The elements of the stepwise S-shaped curve model, including the step height $\triangle\omega_G^j$, the string length s^j for every j-th brick, the number of bricks/steps N_{b} and the range of stiffness degradation $G_0^{\mathrm{ref}} - G_{\mathrm{tmin}}^{\mathrm{ref}}$, may also be chosen in other ways, e.g. based on the direct results of laboratory tests or by using a different continuous model. The stepwise model used here involves $N_{\mathrm{b}} = 10$ bricks to trace the strain history with equal step heights called the stiffness proportions:

$$\Delta\omega_G = \frac{G_0^{\mathrm{ref}} - G_{\mathrm{tmin}}^{\mathrm{ref}}}{N_{\mathrm{b}} G_0^{\mathrm{ref}}}. \tag{12}$$

The string length s^j for every j-th brick ($j = 1..N_{\mathrm{b}}$) is calculated from:

$$s^j = \frac{7}{3}\|\boldsymbol{\varepsilon}\|_{\mathrm{sh}}\left(\sqrt{\frac{1}{1.0 - j\Delta\omega_G + 0.5\Delta\omega_G}} - 1\right). \tag{13}$$

In the numerical simulations, the initial locations of all bricks $\boldsymbol{\varepsilon}^{\mathrm{b}j}$ and the man $\boldsymbol{\varepsilon}$ are usually chosen at the origin of strain space and $\boldsymbol{\varepsilon}^{\mathrm{b}j} = \boldsymbol{\varepsilon} = \mathbf{0}$. All presented simulations are performed with a displacement-based FE program [5]. Hence, in the stress integration procedure, the strain increment $\Delta\boldsymbol{\varepsilon}$ is known. First, the following condition is checked for every j-th brick:

$$d^j = \|\boldsymbol{\varepsilon} + \Delta\boldsymbol{\varepsilon} - \boldsymbol{\varepsilon}^{\mathrm{b}j}\| > s^j. \tag{14}$$

When the distance d^j exceeds the string length s^j, the j-th brick is assumed active and its location should be updated by the following strain increment:

$$\Delta\boldsymbol{\varepsilon}^{\mathrm{b}j} = (\boldsymbol{\varepsilon} + \Delta\boldsymbol{\varepsilon} - \boldsymbol{\varepsilon}^{\mathrm{b}j})\frac{d^j - s^j}{d^j}. \tag{15}$$

11

Once the number of the active bricks n_{ab} is counted, the current tangent reference modulus can be determined:

$$G_{\mathrm{t}}^{\mathrm{ref}} = G_0^{\mathrm{ref}}(1 - n_{\mathrm{ab}}\Delta\omega_G). \tag{16}$$

It is used to calculate the components of the hyperelastic stiffness matrix and, consequently, the stress increment $\Delta\boldsymbol{\sigma}$. In the implementation algorithm of the models for small and intermediate strains, it is important to introduce a substepping scheme since, generally, large strain increments can be delivered from the main program. Small increments of the loading are needed to avoid the overshooting of the nonlinear stiffness changes. In the calculations presented in this article, the substepping is used for the strain increments of Euclidean norm ($\|\Delta\boldsymbol{\varepsilon}\| = \sqrt{\Delta\varepsilon_{ij}\Delta\varepsilon_{ij}}$) that are larger than 10^{-5}.

2.3. Shear strength criterion

In the original BRICK model by Simpson [36, 11], the shear strength is reproduced correctly, i.e. the mobilised friction angle cannot exceed the prescribed maximum friction angle. In the proposed formulation, the shear strength is controlled by the conventional stress-based isotropic Matsuoka-Nakai criterion [25]:

$$F_{\mathrm{MN}}(\boldsymbol{\sigma}) = I_1 I_2 - \frac{9 - \sin^2\phi}{-1 + \sin^2\phi} I_3 \le 0, \tag{17}$$

where ϕ is the effective maximum friction angle and I_1, I_2, I_3 are the stress invariants defined as:

$$I_1 = \sigma_{kk}, \; I_2 = \frac{1}{2}\left[\sigma_{ij}\sigma_{ij} - (I_1)^2\right], \; I_3 = \det(\boldsymbol{\sigma}). \tag{18}$$

To introduce the effective cohesion parameter c, one should calculate the stress invariants in Eq. 18 for the stress state $\boldsymbol{\sigma} - p_{\mathrm{c}}\boldsymbol{\delta}$ with $p_{\mathrm{c}} = c\cot\phi$. Additionally, the admissible stress states are limited by the Rankine tension cut-off criterion $p \ge p_{\mathrm{te}}$.

The flow rule is obtained from the Drucker-Prager plastic potential:

$$G_{\mathrm{DP}}(\boldsymbol{\sigma}) = q - \frac{6\sin\psi}{3 - \sin\psi} p, \tag{19}$$

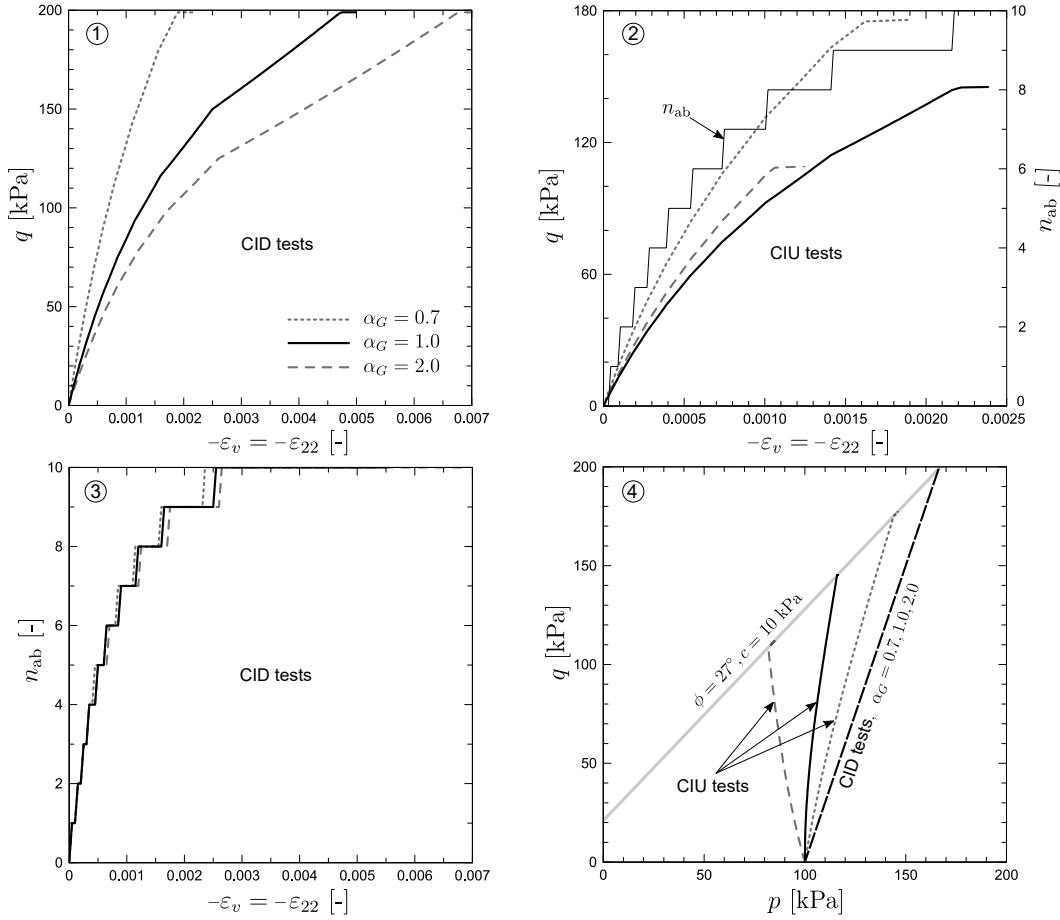where ψ is the dilatancy angle.

12

Figure 5: Simulation of triaxial CID and CIU element tests. 1,2: compression curves $\varepsilon_v - q$ for different values of α_G and drainage conditions. Undrained compression is strain-controlled, so the activation of bricks is independent of α_G and the single $\varepsilon_v - n_{ab}$ curve is plotted together with $\varepsilon_v - q$ curves. 3: drained compression is stress-controlled and the activation of bricks is shown in a separate graph. 4: stress paths in $p - q$ plane for all performed element tests.

When the stress state calculated in the BRICK part of the model (Sect. 2.2) does not obey the shear strength criterion from Eq. 17, it is returned to the yield surface $F_{MN} = 0$. To this end, the implicit return mapping algorithm is applied as described in [20]. The use of the shear strength criterion in the stress space together with the strain-based stiffness degradation model may result in a non-smooth arrival at the deviatoric stress limit. This issue may be minimised by a careful estimation of $\|\boldsymbol{\varepsilon}\|_{sh}$.

2.4. Exemplary element tests

The proposed constitutive model was verified in [7, 9] with selected laboratory test results from the literature for various strain thresholds. In this section, the response of the model at the

13

initial isotropic pressure $p_0 = p_{\text{ref}} = 100$ kPa in triaxial drained (CID) and undrained (CIU) compression is shown. The following values of the material parameters are used:

- Small strain stiffness: $G_{0vh}^{\text{ref}} = 50000$ kPa, $\beta = 0.5$, $\alpha_G = 0.7, 1.0, 2.0$, $p_{\text{ref}} = 100$ kPa;

- Stiffness degradation: $N_{\text{b}} = 10$, $G_{vht\text{min}}^{\text{ref}} = 0.1 \cdot G_{0vh}^{\text{ref}} = 5000$ kPa, $\|\boldsymbol{\varepsilon}\|_{\text{sh}} = 0.0007$;

- Shear strength criterion: $\phi = 27°$, $c = 10$ kPa, $\psi = 5°$, $p_{\text{te}} = 0$ kPa.

The same values are used in the numerical simulations in Sect. 3. The main objective of the element tests is to show the influence of the inherent cross-anisotropy on the triaxial compression. Hence, all material parameters are fixed, except for the coefficient α_G. The results are presented in Fig. 5. In the drained compression, the axial stiffness is inversely proportional to α_G (note that comparison is shown for fixed G_{0vh}^{ref} and not the Young's modulus E_{0v}). In the undrained compression, the shear strength is inversely proportional to α_G as it influences the effective stress paths.

3. Simple example of a tunnelling problem

A simple BVP is analysed. A homogeneous soil around the tunnel is assumed in order to focus on the influence of the coefficient of inherent cross-anisotropy α_G and the initial K_0 stress state on the deformation induced during the tunnel construction in undrained conditions. Assuming the same geometrical and material properties, both the plane strain (2D, 15-node triangle elements) and three-dimensional (3D, 10-node tetrahedral elements) FE models are prepared for numerical analyses. There is no regularisation procedure accessible in the used FE code [5]. To minimise the mesh dependency, first, a possibly fine regular mesh was applied in the whole analysed domain. Then, the mesh of domains far from the tunnel was coarsened until the results started to change substantially.

3.1. 2D model

In the 2D model presented in Fig. 6, a 5.0-m-diameter tunnel with a 0.2-m-thick concrete liner is situated at two different depths: with 16.0 m (deep tunnel) and 9.0 m (shallow tunnel) soil overburden. Symmetry of the problem is taken into account and only the half of the tunnel structure is considered. The dimensions of the model boundary are 50.0 x 31.0 m. The
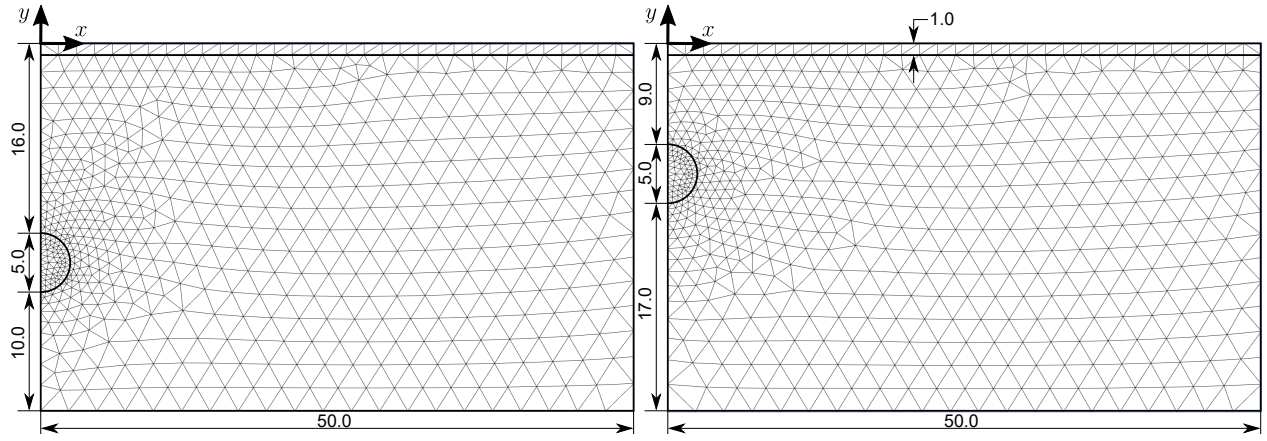
Figure 6: Geometry and FE mesh of the analysed tunnel problem in plane strain conditions (deep tunnel: 1213 15-node triangular elements, 9992 nodes, shallow tunnel: 1162 15-node triangular elements, 9578 nodes).

behaviour of a 30.0 m thick stiff clay layer is described by the proposed anisotropic model with $\gamma_{\text{sat}} = 20.0 \, \text{kN/m}^3$ assuming undrained conditions. The upper granular fill layer of 1.0 m thickness is described by the standard Mohr-Coulomb material to avoid the low level stress dependency of stiffness. Drained conditions are assumed and the parameter values are: $\phi = 30°$, $c = 3.0$ kPa, $\psi = 0.0°$, $E = 70000$ kPa, $\nu = 0.2$, $\gamma = 18.0 \, \text{kN/m}^3$. The groundwater table is located 1.0 m under the ground surface and the soil below is presumed fully saturated. Closed groundwater flow conditions are applied at the bottom and sides of the analysed area. The TBM tunnelling is simulated using the lining contraction method, which is the standard tool for such purposes in the employed FE code [5]. In the first calculation phase, the tunnel lining is introduced by the activation of plate elements (concrete, thickness 0.2 m, $EA = 6 \cdot 10^6 \, \text{kN/m}$, $EI = 20 \cdot 10^3 \, \text{kPa/m}$) with the surrounding interface elements. Simultaneously, soil elements and water pressure are deactivated inside the tunnel perimeter. In the next calculation phase, the contraction of 1.0 % is applied to the tunnel lining.

The influence of pure initial inherent cross-anisotropy is investigated in the tunnelling simulations with the initial isotropic stress condtition $K_0 = 1.0$. Different values of the cross-anisotropy coefficient $\alpha_G = 0.7, 1.0, 2.0, 3.0$ are examined. The obtained deformation in the case of deep tunnel is illustrated in Fig. 7 by settlement troughs and horizontal displacement component profiles in the selected horizontal and vertical cross-sections, respectively. The influence of α_G is evident. In the case of surface settlement profile (along $y = -1.5$ m), the steepness and depth of the trough are proportional to the value of α_G. This dependence is similar along
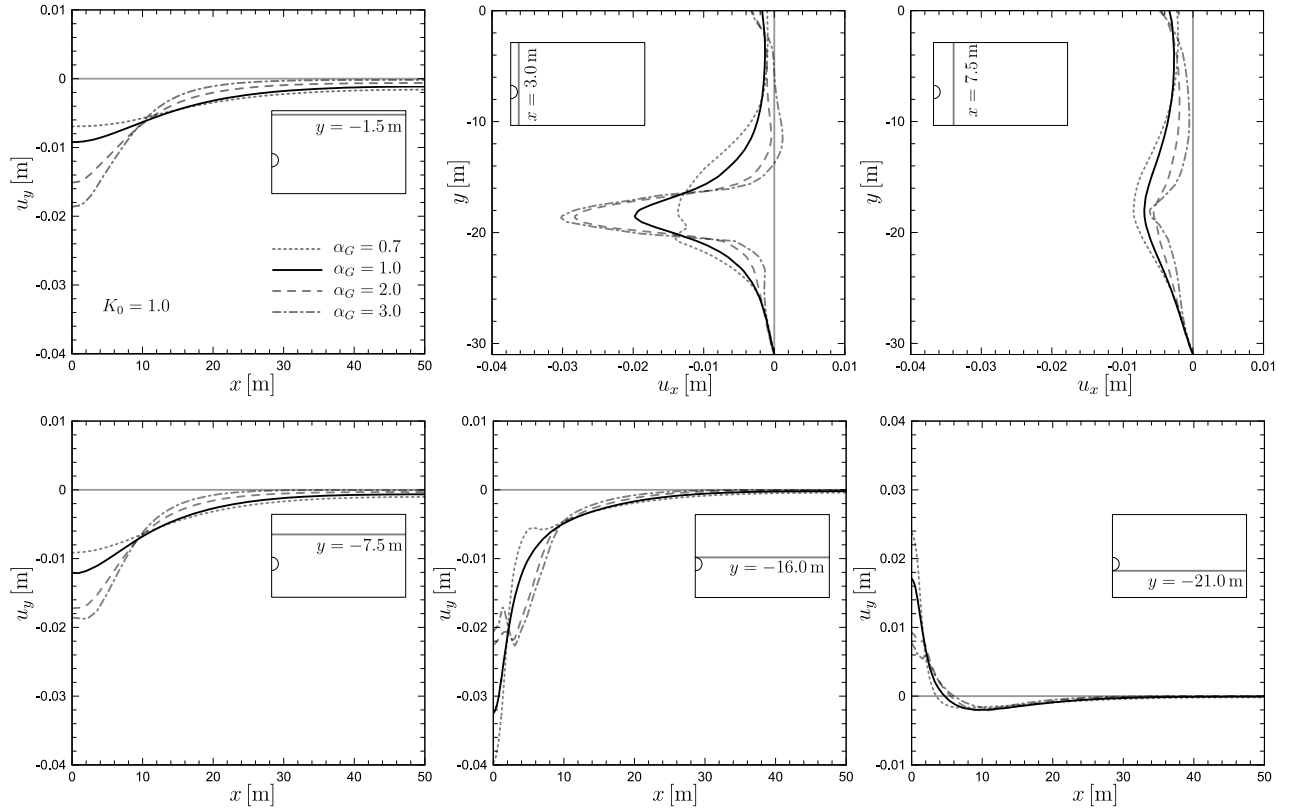
15

Figure 7: Deep tunnel, settlement u_y and horizontal displacement component u_x profiles along the selected horizontal and vertical cross-sections, respectively. The initial isotropic stress state $K_0 = 1.0$ and different values of the inherent cross-anisotropy coefficient α_G.

the horizontal cross-section $y = -7.5\,\mathrm{m}$; however, it inverses in the deeper cross-sections directly above ($y = -16.0\,\mathrm{m}$) and below ($y = -21.0\,\mathrm{m}$) the tunnel lining. Furthermore, the deep settlement troughs are not smooth for high values of α_G in the vicinity of the tunnel. Regarding horizontal displacement profiles, the intensity of horizontal deformation is compatible with settlement, i.e. in the tunnel vicinity ($x = 3.0\,\mathrm{m}$) larger α_G induces larger lateral deflection. This relationship becomes inverse in the vertical cross-section located $5.0\,\mathrm{m}$ from the tunnel lining (along $x = 7.5\,\mathrm{m}$).

The initial inherent cross-anisotropy influences also the maps of stiffness degradation. It is illustrated in Fig. 8 by filled contour plots of the active bricks number n_{ab} obtained for $K_0 = 1.0$ and three values of $\alpha_G = 0.7, 1.0, 2.0$. In the case of higher horizontal stiffness ($\alpha_G = 2.0$), some zones of localised unloading ($n_{\mathrm{ab}} = 0$) are visible in the close neighbourhood of the tunnel.

The hyperelastic kernel reproduces the pure stress-induced anisotropy of the stiffness for $\alpha_G = 1.0$ and anisotropic stress states. In order to inspect the influence of pure stress-induced
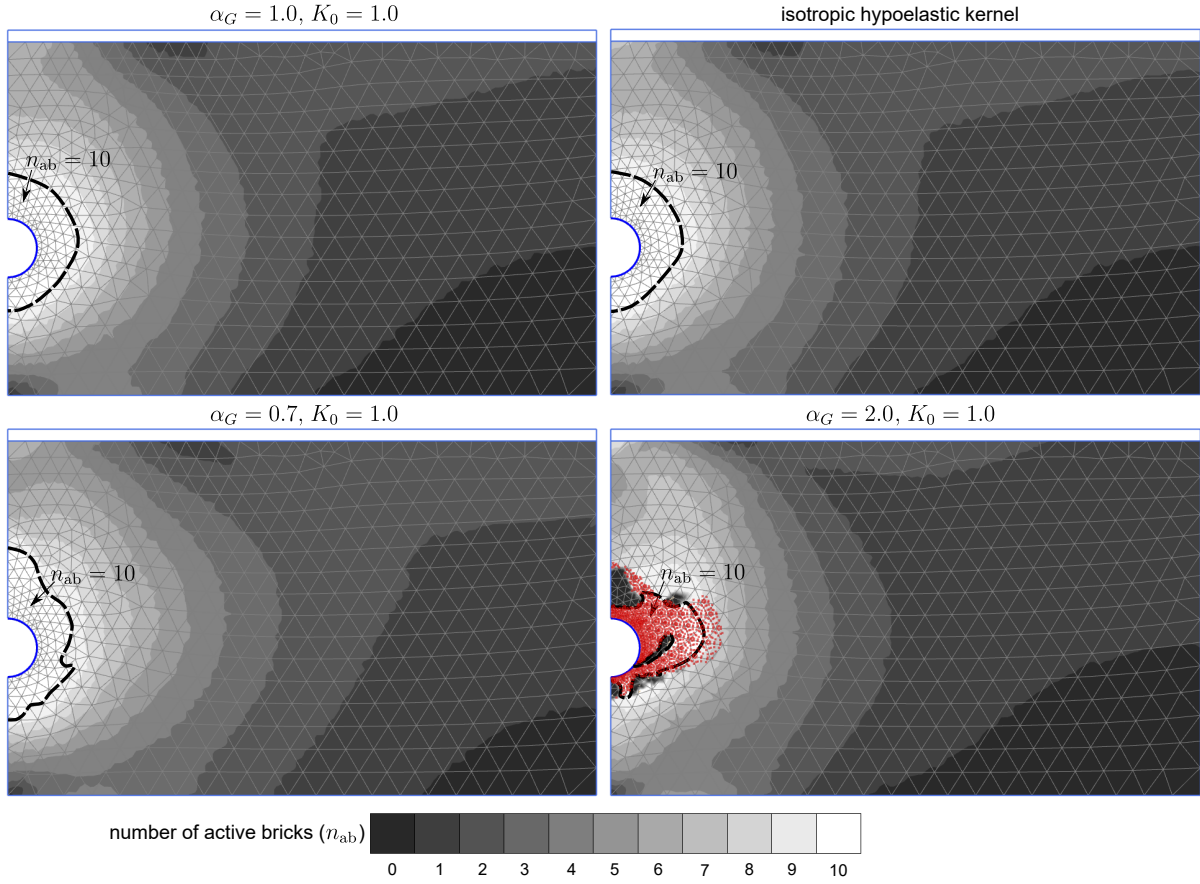
16

Figure 8: Deep tunnel, maps of stiffness degradation obtained for $K_0 = 1.0$ and different values of α_G. The response of the model with purely isotropic hypoelastic kernel is shown for comparison. The intensity of stiffness degradation is indicated by the number of active bricks n_{ab} computed after the undrained tunnel contraction phase. In the subfigure for $\alpha_G = 2.0$, the red plastic points that indicate stress states reaching the shear strength criterion are shown additionally. This allows to see the connection with the dark regions where unloading of all bricks occurs close to the intensive shear zones.

anisotropy in the analysed tunnelling BVP, a reference isotropic stiffness needs to be introduced as the small strain kernel. Moreover, such isotropic stiffness should be barotropic, i.e. dependent on the mean stress level (not stress obliquity). This may be accomplished by using the hypoelastic formulation based on the Hooke's linear elastic stiffness with the constant Poisson's ratio ν_0 and the stress-dependent small strain Young's modulus:

$$E_0(\boldsymbol{\sigma}) = E_0^{\mathrm{ref}} \left(\frac{p}{p_{\mathrm{ref}}} \right)^m, \tag{20}$$

where E_0^{ref} is the reference Young's modulus at the reference mean stress $p = p_{\mathrm{ref}}$ and m is the exponent in the above power law. Choosing the parameter values: $E_0^{\mathrm{ref}} = 120000$ kPa, $\nu_0 = 0.2$, $m = 0.5$, $p_{\mathrm{ref}} = 100$ kPa and mean stress level p_0, the initial hypoelastic stiffness is the same
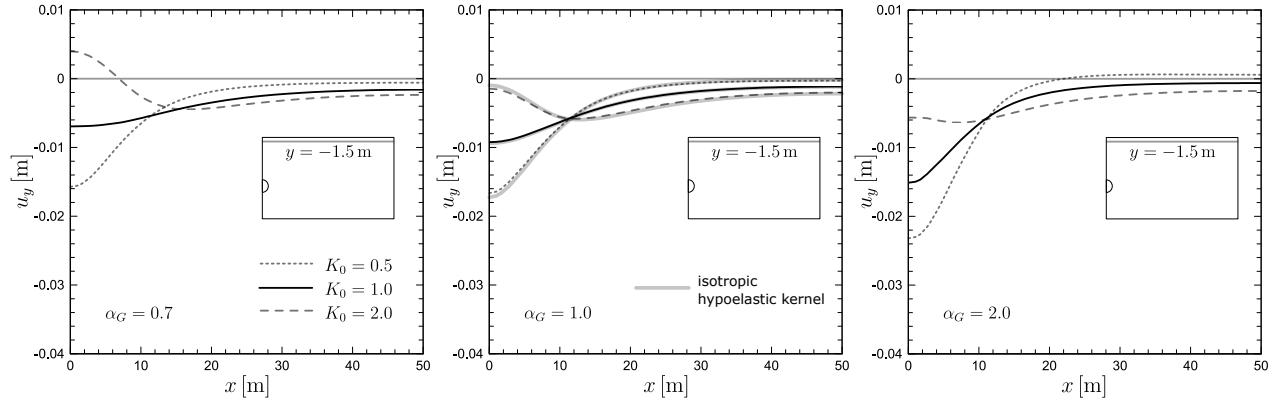
Figure 9: Deep tunnel, comparison of the surface settlement u_y profiles for different values of the initial stress ratio K_0 and the inherent cross-anisotropy coefficient α_G.

as in the case of hyperelastic model for the isotropic stress $\sigma_0 = p_0 \operatorname{diag}(1,1,1)$, $\alpha_G = 1.0$ and remaining parameter values fixed in the numerical simulations (Sect. 2.4).

The BRICK stiffness degradation procedure in the reference isotropic model controls the current value of the tangent Young's modulus E_t^{ref}. Its minimum value is selected likewise in the anisotropic model, i.e. $E_{0min}^{\text{ref}} = 0.1 \cdot E_0^{\text{ref}} = 12000$ kPa.

The results of numerical simulations with the isotropic hypoelastic kernel are compared with those obtained using the anisotropic hyperelastic kernel (without incorporation of the inherent cross-anisotropy, $\alpha_G = 1.0$). This is shown for the maps of stiffness degradation and $K_0 = 1.0$ in Fig. 8 and for the surface settlement troughs and three values of $K_0 = 0.5, 1.0, 2.0$ in Fig. 9. The influence of pure stress-induced anisotropy of stiffness in the analysed tunnelling BVP occurs to be of a minor importance. The differences in the stiffness degradation maps and settlement troughs for the isotropic hypoelastic and the anisotropic hyperelastic ($\alpha_G = 1.0$) small strain kernels are insignificant from the practical point of view.

The comparison of surface settlement troughs in Fig. 9 is presented to show the influence of initial K_0 stress state on the tunnelling-induced deformation. This is performed for three values of the inherent cross-anisotropy coefficient, $\alpha_G = 0.7, 1.0, 2.0$. The depth and steepness of the obtained surface settlement troughs are inversely proportional to the K_0 value, and the largest settlement is obtained for $K_0 = 0.5$ for all examined α_G coefficients. The largest absolute settlement is obtained for $K_0 = 0.5$ and $\alpha_G = 2.0$. In the case of $K_0 = 2.0$, the shape of settlement troughs becomes convex upwards above the tunnel, and for $\alpha_G = 0.7$ even uplift over the initial ground level is obtained.
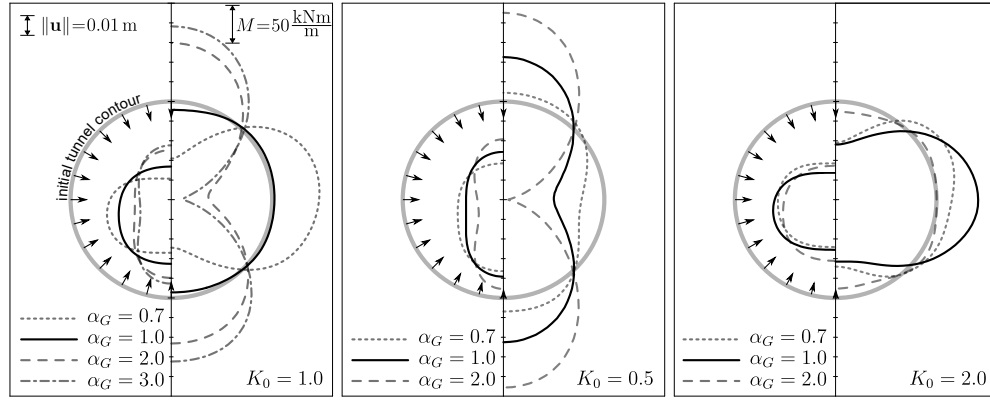
18

Figure 10: Deep tunnel lining, comparison of total displacement $\|\mathbf{u}\|$ (left-hand side of each graph) and bending moments M (right-hand side of each graph) polar diagrams for different values of the initial stress ratio K_0 and the inherent cross-anisotropy coefficient α_G.

The deformation and bending of the deep tunnel lining are presented in Fig. 10 for all analysed 2D cases. Under initial isotropic stress condition ($K_0 = 1.0$), the ovalisation of the tunnel lining is vertical for $\alpha_G > 1.0$ and horizontal for $\alpha_G < 1.0$. For $\alpha_G = 1.0$, the deformed shape of the tunnel lining remains almost circular after the contraction and the bending moments are negligible when compared with simulation results for assumed inherent cross-anisotropy ($\alpha_G \neq 1.0$). In the case of higher initial vertical stress component ($K_0 = 0.5$), the tunnel ovalisation is vertical regardless of the examined α_G values. For the higher initial horizontal stress component ($K_0 = 2.0$) and $\alpha_G = 0.7, 1.0$, the ovalisation is horizontal. In the simulation with $K_0 = 2.0$ and $\alpha_G = 2.0$ the tunnel contracts almost isotropically with small bending moments.

The same plan of FE numerical simulations is performed for the shallow tunnel geometry. The influence of the pure initial inherent anisotropy on profiles of the vertical and horizontal displacement components in the selected cross-sections is presented in Fig. 11. The general mode of deformation and its dependency on α_G are similar to those observed for the deep tunnel. The main differences concern the smoothness of the displacement profiles. It is particularly evident for the surface settlement troughs and can be explained by the small distance between the tunnel and the ground level where localised shear zones occur. The influence of K_0 on the surface settlement troughs is presented in Fig. 12. The intensity of deformation is larger as compared with the analogous results of deep tunnel simulations in Fig. 9. In the case of $K_0 = 2.0$, a much more pronounced heave is observed in the horizontal section above the tunnel.
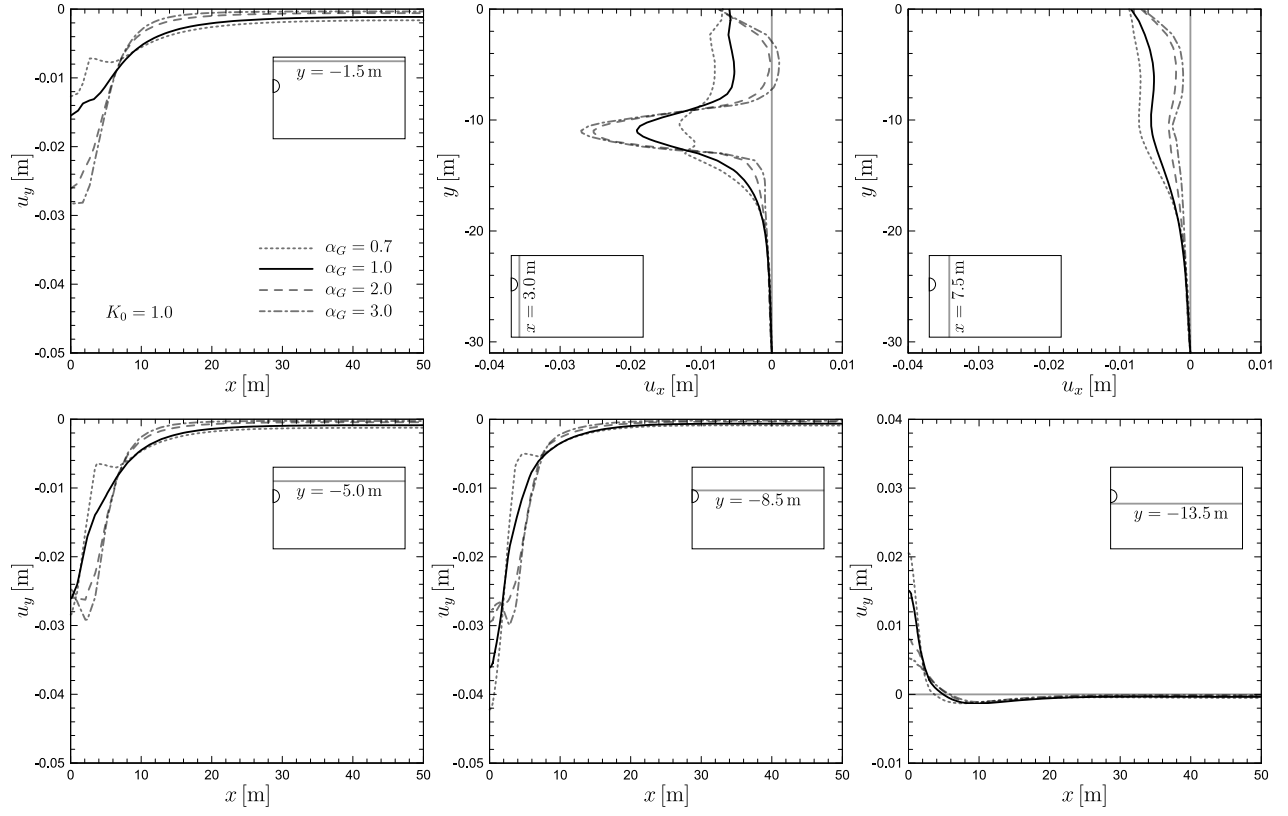
19

Figure 11: Shallow tunnel, settlement u_y and horizontal displacement component u_x profiles along the selected cross-sections. Initial isotropic stress state $K_0 = 1.0$ and different values of the inherent cross-anisotropy coefficient α_G.
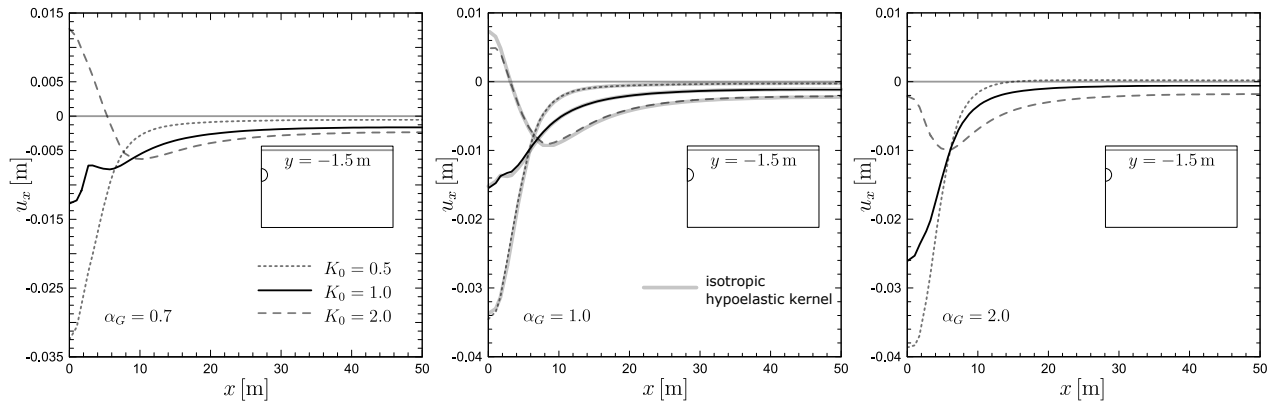

Figure 12: Shallow tunnel, comparison of surface settlement u_y profiles for different values of the initial stress ratio K_0 and the inherent cross-anisotropy coefficient α_G.
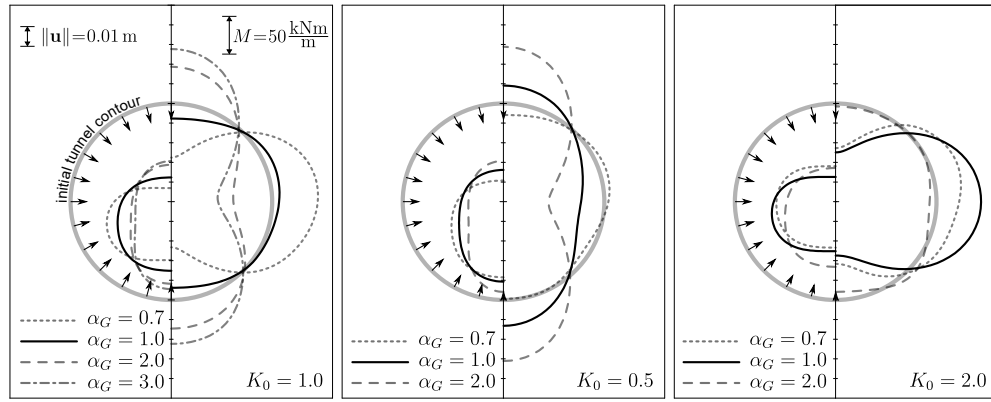
20

Figure 13: Shallow tunnel lining, comparison of total displacement $\|\mathbf{u}\|$ (left-hand side of each graph) and bending moments M (right-hand side of each graph) polar diagrams for different values of the initial stress ratio K_0 and the inherent cross-anisotropy coefficient α_G.
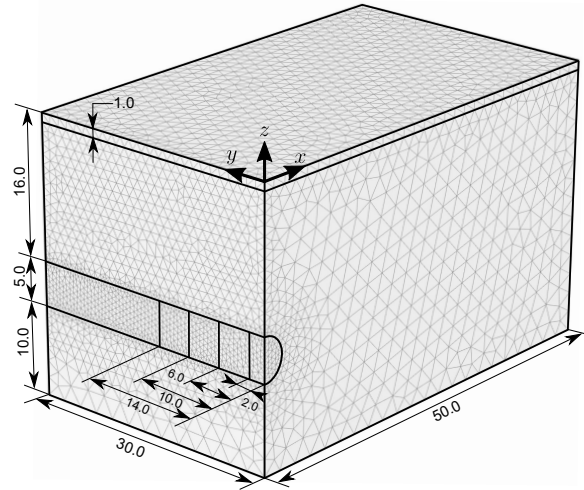

Figure 14: Geometry and FE mesh of the exemplary single tunnel problem in 3D conditions. Only the deep tunnel case is analysed which is analogous to the model in plane strain conditions (42538 10-node tetrahedral elements, 67659 nodes).

The deformation and bending of the shallow tunnel lining are presented in Fig. 13 for all analysed 2D cases. Qualitatively, there are just minor variations from the comparable results for the deep tunnel shown in Fig. 10, whereas quantitatively the largest differences between the deep and shallow tunnels are observed for the initial stress states $K_0 = 0.5$ and $K_0 = 1.0$.

3.2. 3D model

The geometry of the 3D model, presented in Fig. 14, is obtained by 30 m extrusion of the 2D model cross-section in the horizontal direction keeping the similar mesh density. In the
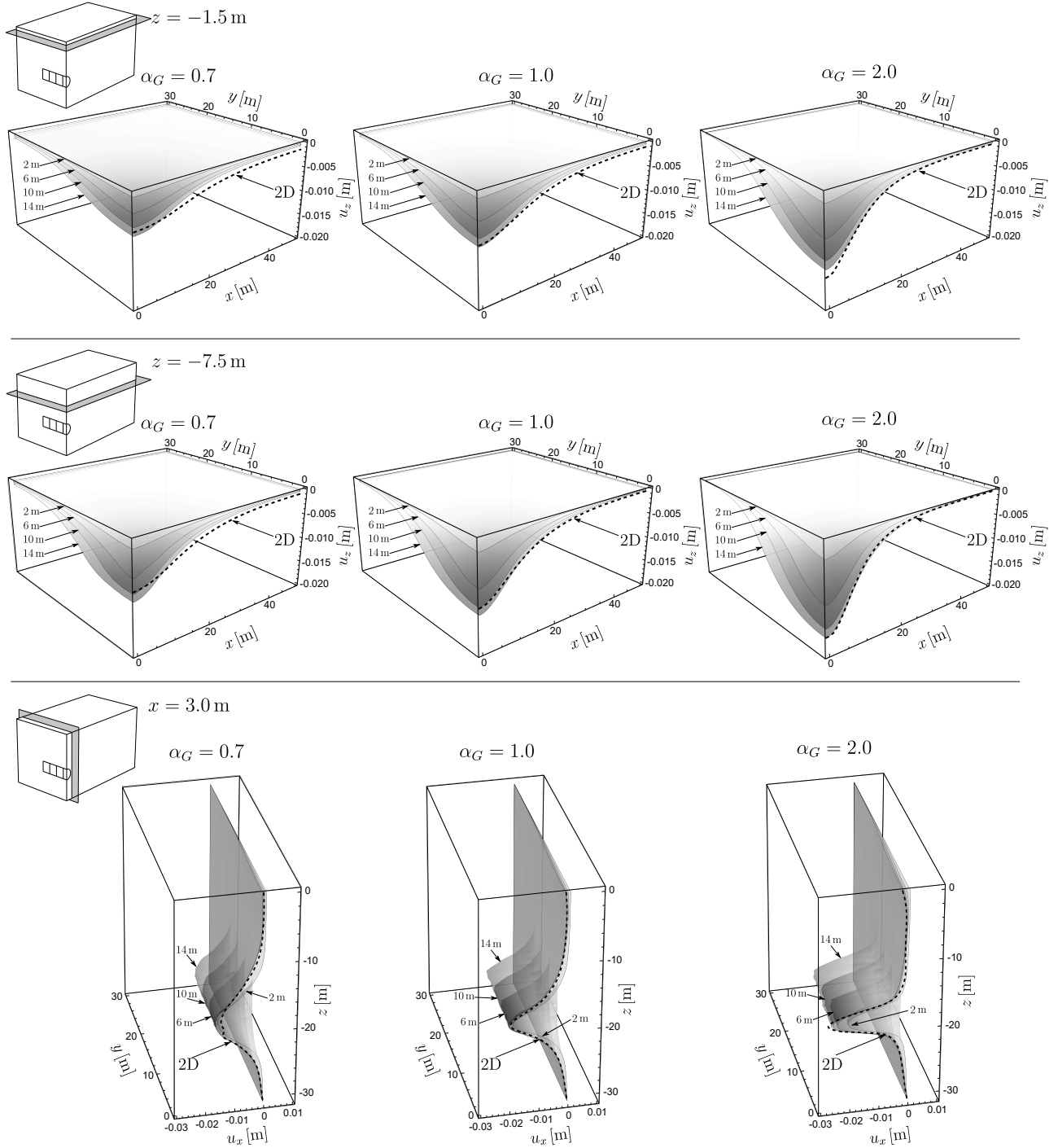
21

Figure 15: Settlement u_z and horizontal displacement component u_x surface plots in the selected cross-sectional planes obtained in 3D model. The initial isotropic stress state $K_0 = 1.0$ and different values of the inherent cross-anisotropy coefficient α_G are selected. In each graph, the deformations are shown after one-step introduction of 2, 6, 10 and 14 m long single tunnel sections followed by 1.0 % contraction of the lining.

22

3D version of the applied FE code [5], the vertical axis is $\mathbf{v} = [0, 0, 1]^T$, which leads to the anisotropic microstructure tensor $\mathbf{M} = \mathrm{diag}(0, 0, 1)$, according to Eq. 3. The main aim of the 3D simulations is to analyse the influence of principal stress rotations occurring at the front of the tunnel on the deformation under different degrees of the inherent cross-anisotropy. Moreover, it was important to confront the 3D results with those obtained in the 2D model using a similar method of tunnel contraction. Only FE simulations of the deep tunnel for initial isotropic stress ($K_0 = 1.0$) and three values of the inherent cross-anisotropy coefficient $\alpha_G = 0.7, 1.0, 2.0$ are performed. The tunnel is introduced in the simulations as a single segment of four different lengths (2, 6, 10 and 14 m) indicated in Fig. 14. The tunnelling simulation procedure, based on 1.0% contraction of the lining, is analogous to that applied in the 2D model. The only exception is the application of the distributed horizontal loading in order to support the front of the tunnel. From the top to the bottom of the tunnel's front, a total normal stress varying from 170 kPa up to 230 kPa is applied.

The obtained deformation is illustrated in Fig. 15 by settlement troughs and surface plots of the horizontal displacement component in the selected two horizontal and one vertical cross-sectional planes, respectively. The corresponding results of the 2D calculations are also shown in Fig. 15 by the dashed settlement troughs placed in the front faces of the 3D graphs. As expected, increasing the length of tunnelling segment results in deeper settlement troughs and for the longest segment (14 m) the results agree well with those obtained in the 2D simulations. The deformation occurring in the vicinity of the tunnel lining after the contraction phase in undrained conditions is illustrated by surface plots of u_x in the vertical plane located at $x = 3.0$ m from the symmetry plane of the model. In the case of $\alpha_G = 0.7$ and the inherent isotropy $\alpha_G = 1.0$, the magnitude of this deformation is almost equal regardless of the segment length. The influence of the segment length on the u_x surface plots is, however, evident for $\alpha_G = 2.0$. The horizontal deformation obtained in the 2D calculations is reached for the longest tunnel segment (14 m).

4. St James's tunnelling case study

The construction of twin tunnels of the Jubilee Line Extension project at St James's Park in London is back analysed with the proposed anisotropic hyperelastic-plastic constitutive model used for London Clay. The results of field measurements at St James's Park are often used for
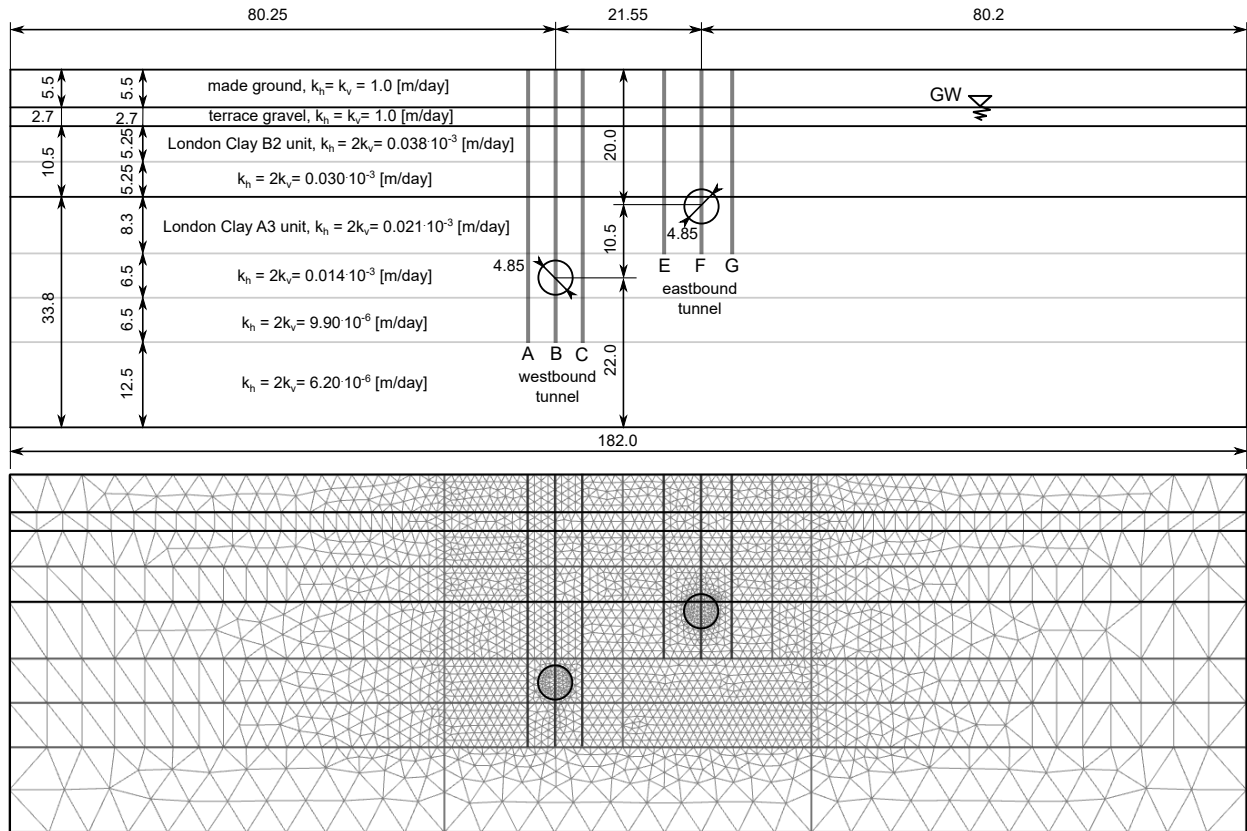
23

Figure 16: Geometry and FE mesh of the back analysed case study of twin tunnels in London Clay at St James's Park (5682 15-node triangular elements, 45985 nodes). The position of measuring instrumentation (rod extensometers and electrolevel inclinometers in axes A-C and E-G) is shown.

the validation of soil models and tunnelling simulation methods [1, 12, 15, 47, 3, 42, 21]. This is a very well-instrumented and documented case study. The field measurement results are available in reports [32, 41] with extensive supporting data on the mechanical characteristics of London Clay in, e.g. [13, 31, 14, 19].

4.1. FE model

The applied 2D model geometry and FE mesh, with the boundary dimensions of 182.0×52.5 m, is shown in Fig. 16. The model geometry is adopted from [1, 3]. Two tunnels, with the diameter of 4.85 m and 0.17 m thick concrete lining, were constructed using an open-face shield and excavated by mechanical backhoe in London Clay. The tunnel axes in the analysed cross-section are at the depths of 30.5 m and 20.0 m below the ground surface in the case of westbound (WB) and eastbound (EB) tunnels, respectively. The groundwater level is located 5.5 m below the ground surface. London Clay deposit is covered by 2.7 m layer of the terrace gravel and

24

5.5 m layer of the made ground. Closed groundwater flow conditions are applied at the bottom of the analysed rectangular area. The tunnelling simulation procedure, based on the contraction of the lining in the undrained calculation phase, is analogous to that applied in Section 3. The values of tunnel contraction applied in the simulations are equal to the measured volume loss v_L at the ground surface. It follows the assumption that the measured v_L corresponds to the deformation of soil around the tunnel that moves towards the tunnel boundary. Additionally, after the construction of WB and EB tunnels the consolidation calculation phases are included in the simulations according to the real time schedule on the site. During the consolidation phases, seepage groundwater flow conditions are assumed around the tunnel [44].
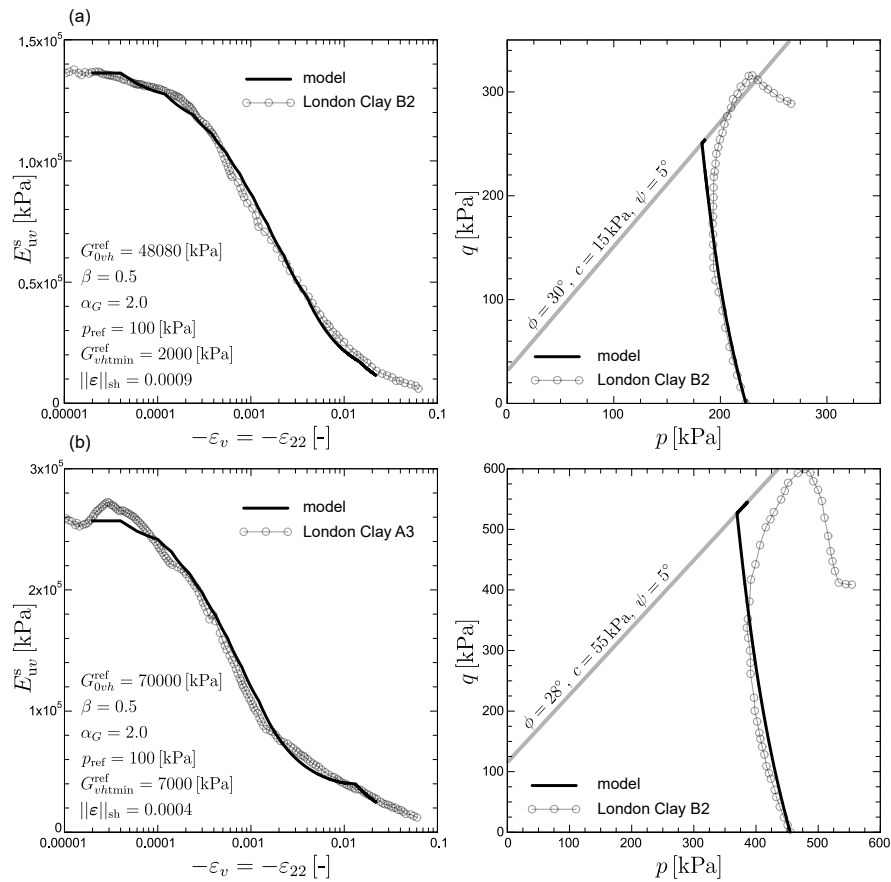

Figure 17: Calibrations of the hyperelastic-plastic model stiffness and strength parameters for London Clay. Element test results are compared to the undrained triaxial compression test results from [19]: (a) London Clay B2 unit (B2c 11 m block sample), (b) London Clay A3 unit (38.71 m sample)

25

Table 1: Parameters of London Clay B2 and A3 units

	Parameter	London Clay B2	London Clay A3
Small strain stiffness	G_{0vh}^{ref} [kPa]	48080	70000
	β [-]	0.5	0.5
	α_G [-]	2.0	2.0
	p_{ref} [kPa]	100	100
Stiffness degradation	$G_{vht\mathrm{min}}^{\mathrm{ref}}$ [kPa]	2000	7000
	$\|\boldsymbol{\varepsilon}\|_{\mathrm{sh}}$ [-]	0.0009	0.0004
Shear strength criterion	ϕ [°]	30	28
	c [kPa]	15	55
	ψ [°]	5	5
	p_{te} [kPa]	0	0
Unit weight and initial stress	γ [kN/m^3]	20.0	20.0
	K_0 [-]	1.0	1.0

4.2. Soil properties

Following the numerical analyses in [1, 3], the made ground is modelled as a linear elastic material ($E = 5000\,\mathrm{kPa}$, $\nu = 0.3$, $\gamma = 18\,\mathrm{kN/m^3}$), terrace gravel is described by the Mohr-Coulomb model ($E = 35000\,\mathrm{kPa}$, $\nu = 0.2$, $\gamma = 20\,\mathrm{kN/m^3}$, $c = 1\,\mathrm{kPa}$, $\phi = 35°$, $\psi = 17.5°$). The initial stress ratio in these cover soil layers is $K_0 = 0.5$.

The mechanical behaviour of London Clay B2 and A3 units is simulated with the proposed anisotropic hyperelastic-plastic material model. A series of undrained triaxial compression element tests were simulated to determine the stiffness and strength parameters for London Clay. The numerical element test results were confronted in the calibration with the results of high quality laboratory tests reported in [14, 19].

According to the findings presented in [19], the average value of the inherent cross-anisotropy coefficient from laboratory tests , $\alpha_G = 2.0$, is chosen. The remaining stiffness parameters, i.e.: $G_{0vh}^{\mathrm{ref}}, \beta, p_{\mathrm{ref}}, \|\boldsymbol{\varepsilon}\|_{\mathrm{sh}}, G_{vht\mathrm{min}}^{\mathrm{ref}}$, are determined by fitting the S-shaped curves of the secant undrained Young's modulus $E_{\mathrm{u}v}^{\mathrm{s}}$ that undergoes the degradation with the vertical strain ε_v. The shear strength softening is not incorporated into the constitutive model and the applied Matsuoka-Nakai [25] shear strength criterion simply represents the peak envelope. Hence, unlike in the critical state models, the effective cohesion parameter is used here. The shear strength parameters of London Clay units are obtained by fitting the strength envelope to the undrained compression stress paths. The fitting of S-shaped curves and undrained stress paths for laboratory tests on B2 and A3 London Clay units is presented in Fig. 17.

26

Still the most difficult initial state parameter to be determined for the overconsolidated clay deposits is the initial stress ratio K_0. Its value is influenced by the geological history which is not easy to describe and simulate accurately. On the other hand, the interpretation of K_0 from in situ measurements is difficult due to the evident stiffness anisotropy. In the numerical analyses presented by Addenbrooke et al. [1], the constant initial stress ratio $K_0 = 1.5$ is adopted in London Clay from the upper-bound profile given by Hight and Higgins [18] for depths between 10 and 30 m below the ground surface. Grammatikopoulou et al. [16] and Avgerinos et al. [3] used kinematic hardening soil models to simulate the deposition and overloading/unloading history. They obtained variable depth-K_0 profiles. In both cases K_0 is almost constant with the average value close to 1.0 within the deeper part of A3 unit. The variability of K_0 within the B2 unit is larger and its value approaches 0.5 directly below the bottom of the terrace gravel. The anisotropic model presented in the paper is designed for modelling stiff overconsolidated soils, and it is not capable to simulate normally consolidated state properly. Therefore, the initial stress state should be prescribed for the current geometry of geological layers. In the presented numerical simulations of the St James's case study, the initial stress ratio is $K_0 = 1.0$ for the both London Clay units.

The values of all parameters of the anisotropic hyperelastic-plastic model for London Clay units B2 and A3 are listed in Table 1. The permeability in London Clay is anisotropic and decreases with depth. The values of permeability coefficients, adopted from [1] for the separated London Clay layers and cover soils, are shown in Fig. 16.

4.3. Calculations and results

The following calculation phases were performed in the numerical analysis:

- Initiation of state variables, hydrostatic pore water pressure, and K_0 stress conditions;

- WB tunnel construction, application of contraction in undrained conditions;

- Consolidation phase, $\Delta t = 256$ days;

- EB tunnel construction, application of contraction in undrained conditions;

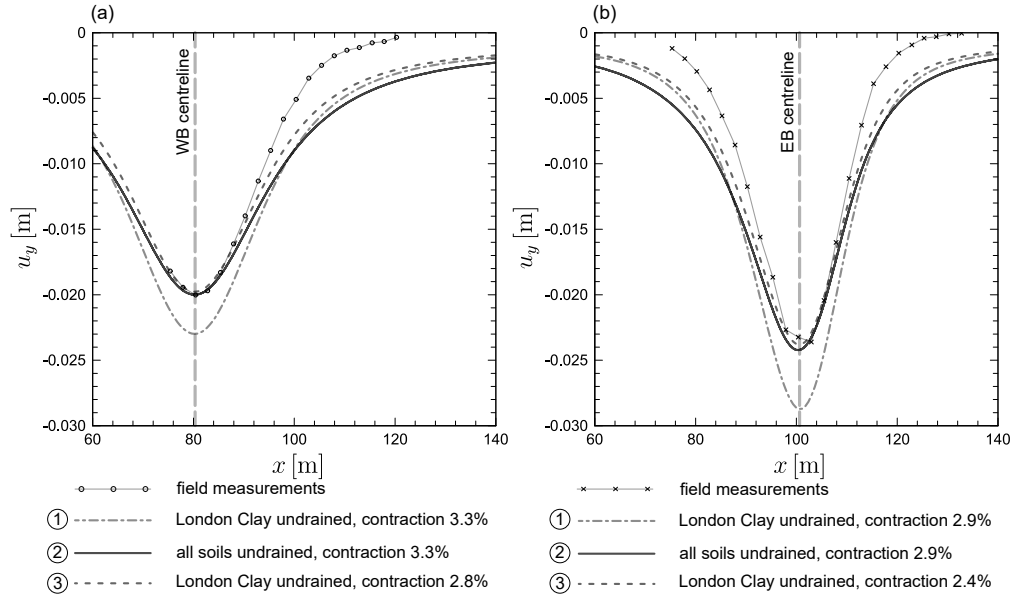- Three consolidation phases, $\Delta t = 415, 3440, 1831$ days.

Figure 18: Surface settlement troughs after the construction of (a) WB tunnel and (b) EB tunnel. Comparison of field measurements with calculation results from the three modelling variants regarding undrained behaviour of cover soils and tunnel contraction values.

In the FE code used in the calculations [5], the undrained behaviour, i.e. preventing changes of volumetric strain by high bulk modulus of pore water resulting in changes of excess pore pressure, may be selected in the material properties to be active or not during the undrained calculation phase. The values of volume loss prescribed to the tunnel contractions in undrained calculation phases are reported in [32]. In the WB and EB tunnels at St James's Park, the volume losses are 3.3 % and 2.9 %, respectively. These values are remarkably high in comparison with commonly estimated volume losses in similar tunnelling projects. This is discussed by Standing and Burland [40] or more recently by Jovičić et al. [21].

The first investigated aspect of the performed analysis were the immediate settlement troughs induced separately during the WB and EB tunnel constructions. Three different sets of simulation conditions regarding the undrained behaviour of cover soils and the values of tunnel contraction were considered. The calculated settlement troughs for all modelling variants compared with field measurements are shown in Fig. 18.

In the first variant, the undrained behaviour is selected only to the London Clay layers and the cover soils are modelled as drained, the contraction values for the WB and EB tunnels are set to 3.3 % and 2.9 %, respectively, as recommended in [32]. The steepness of the obtained settlement troughs are satisfactory; however, the calculated settlement is higher than

28

the measured in the centrelines for both tunnels, i.e.: 15 % and 21 % for WB and EB tunnels, respectively.

In the second variant of the simulation conditions, the undrained behaviour is chosen for all soil layers while maintaining the recommended high tunnel contractions. In this case, the calculated steepness and depth of the settlement troughs show good agreement with the field measurement.

The cover soils are not fine-grained; hence, it seems reasonable to model them assuming the drained behaviour during the tunnel contraction phases. For this reason, in the third variant of the simulation conditions, undrained behavior is applied only to the London Clay layers and the recommended values of contractions were reduced to give the depths of settlement trough being equal to the measured ones. The lowered contraction values for the WB and EB tunnels are 2.8 % and 2.4 %, respectively. This set of modelling conditions gives the best fit to the measured surface settlement troughs as can be seen in Fig. 18.

In the following, the results of performed numerical simulations are presented for the drained behaviour of cover soils, i.e. for the first and third variant of the modelling conditions. The calculated and measured profiles of displacement components, induced during the tunnel construction phases, in vertical axes A,B,C and E,F,G (shown in Fig. 16) are presented in Figs. 19 and 20 for the WB and EB tunnels, respectively. Generally, a good compatibility is displayed and the calculated displacements are slightly higher than the measured ones. The difference between the displacements calculated with the high and reduced contraction is also not significant from the practical point of view.

The additional deformation during the consolidation phases, i.e. between the WB and EB tunnel constructions and after the EB tunnel construction, is uniform. The comparison of the calculated and measured long-term deformation is shown for the settlement trough located 5.0 m under the ground surface in Fig. 21. The total settlement profiles are shown, i.e. both the settlement induced in the undrained tunnel construction phases and the consolidation settlement, are included. The results of field measurements are taken from [3]. The calculated long-term settlement profiles present satisfactory agreement with the measured ones only during the period of the WB and EB tunnel constructions including 256 days of consolidation. However, the measured settlements during 5686 days (ca. 15.5 years) after the EB tunnel construction are almost two times higher then the calculated. In the calculations, the consolidation settlement
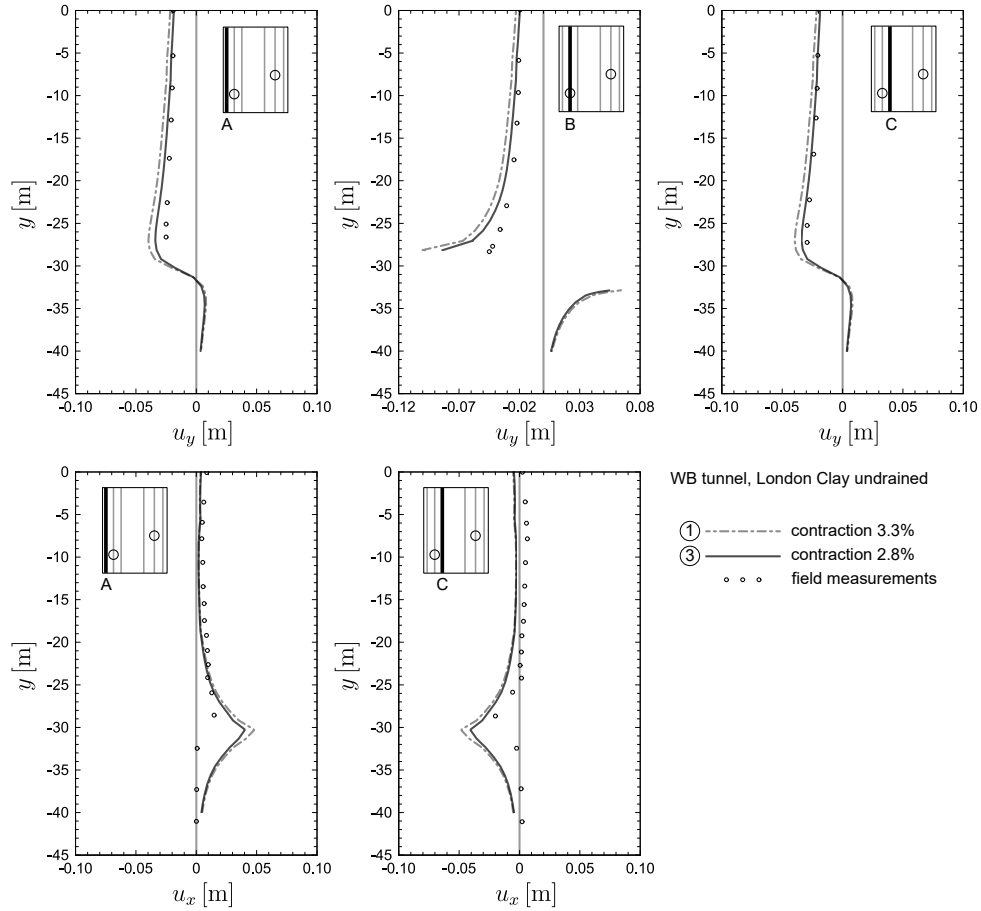
29

Figure 19: The immediate deformation induced during the WB tunnel undrained construction phase: calculated and measured vertical displacement component profiles u_y in axes A,B,C and horizontal displacement component profiles u_x in axes A,C.

is stabilising in 15.5 years, whereas in the field measurements the long-term deformations are still increasing.

5. Conclusions

The application of a new anisotropic hyperelastic-plastic constitutive model for stiff soils in the FE simulations of tunnelling-induced deformation is presented in the article. The structure of the model is simple, and it inherits the one used in the standard elastic-plastic models where admissible stress states are limited only by the conventional shear strength criterion. The most important improvement is the novel material description of the pre-failure barotropic stiffness, which is based on the anisotropic hyperelastic stress-strain relation controlled by the strain based BRICK-type procedure. The number of material constants is not excessive, and the
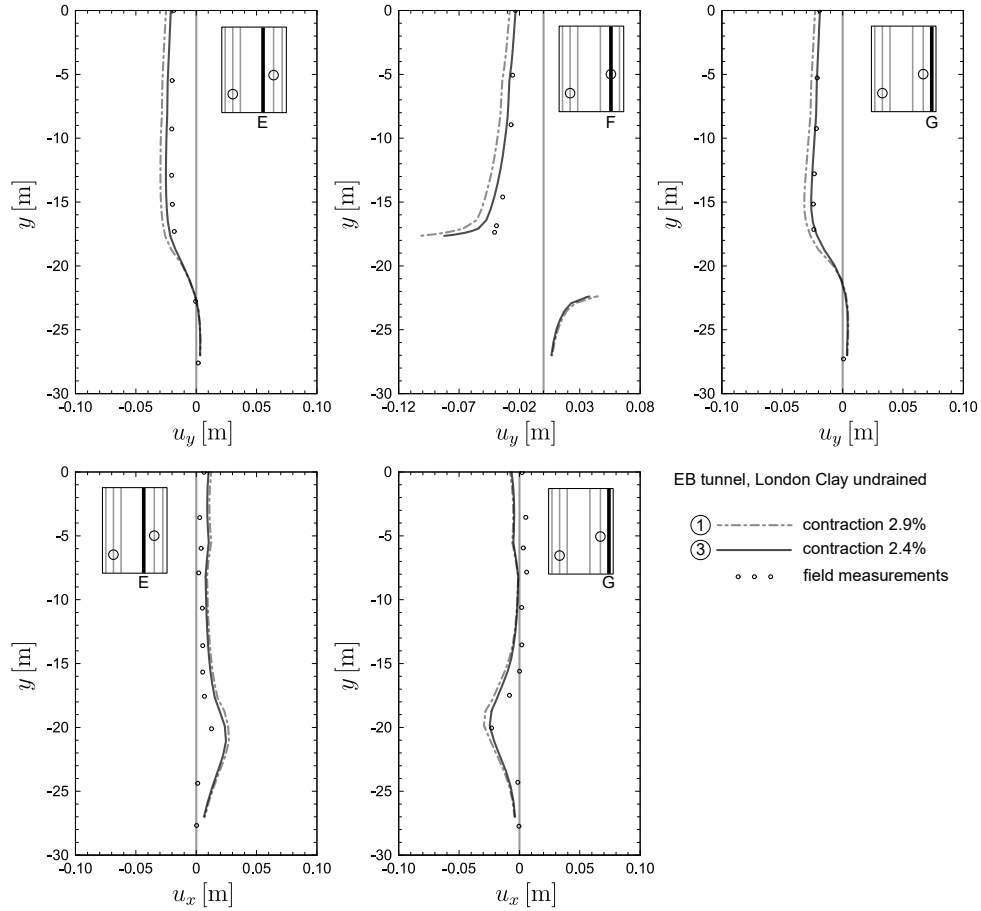
30

Figure 20: The immediate deformation induced during the EB tunnel undrained construction phase: calculated and measured vertical displacement component profiles u_y in axes E,F,G and horizontal displacement component profiles u_x in axes E,G.

model parameters are determinable in the present experimental routines. The results of the conducted FE tunnelling simulations are shown to be in a good agreement with deformation observed in the real cases, judging by field measurements of the surface settlement troughs and displacement field around the tunnel excavations. The final shapes of the settlement troughs are shown to be dependent both on the inherent cross-anisotropy coefficient α_G and the initial stress ratio K_0 values. Nevertheless, the magnitude of the settlement is proportional to the applied tunnel contraction value which is the technological parameter in the modelling of tunnelling-induced deformation. The performance of the model is best in the short-term analyses in soil undrained conditions. This is an important practical aspect as the most unfavourable differential displacements are induced in the short-term undrained conditions. However, the calculated long-term settlements for the analysed tunnelling case study at St James's Park are
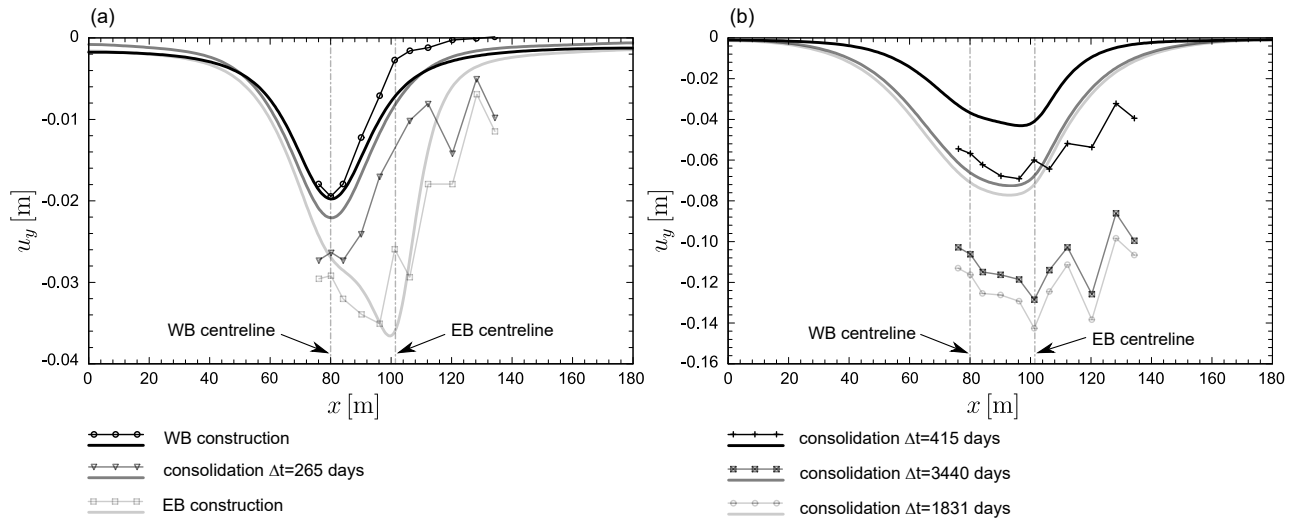
31

Figure 21: Calculated (thick solid lines) and measured long-term total settlements troughs in the horizontal cross-section located 5.0 m under the ground surface. The case with the reduced tunnel contraction is presented: (a) construction period of the WB and EB tunnels, (b) settlements after the EB tunnel construction.

too small, and this problem needs to be improved in the further development of the model. It can be achieved by introduction of a boundary yield surface or surfaces controlled by the evolution of new state variables with a cost of additional material parameters. In the future works, it is planned to take into account the small-strain cross-anisotropy incorporation in the elastic region of the HSBrick model introduced recently in [10].

References

[1] Addenbrooke TI, Potts DM, Puzrin AM (1997) The influence of pre-failure soil stiffness on the numerical analysis of tunnel construction. Géotechnique 47(3):693–712, DOI 10.1680/geot.1997.47.3.693

[2] Amorosi A, Rollo F, Dafalias YF (2021) Relating elastic and plastic fabric anisotropy of clays. Géotechnique 71(7):583–593, DOI 10.1680/jgeot.19.P.134

[3] Avgerinos V, Potts DM, Standing JR (2016) The use of kinematic hardening models for predicting tunnelling-induced ground movements in London Clay. Géotechnique 66(2):106–120, DOI 10.1680/jgeot.15.P.035

[4] Boehler JP, Sawczuk A (1977) On yielding of oriented solids. Archives of Mechanics 27:185–206, DOI 10.1007/BF01180085

32

[5] Brinkgreve RBJ, Kumarswamy S, Swolfs WM, Zampich L, Ragi Manoj N (2023) Plaxis finite element code for soil and rock analyses. Plaxis bv, Bentley Systems, Incorporated

[6] Clarke SD, Hird CC (2012) Modelling of viscous effects in natural clays. Canadian Geotechnical Journal 49:129–140, DOI 10.1139/t11-084

[7] Cudny M (2013) Some aspects of the constitutive modelling of natural fine grained soils. Habilitation Monograph, Faculty of Civil and Environmental Engineering, Gdańsk University of Technology, Wydawnictwo IMOGEOR, available at www.researchgate.net

[8] Cudny M, Partyka E (2017) Influence of anisotropic stiffness in numerical analyses of tunneling and excavation problems in stiff soils. In: Lee W, Lee JS, Kim HK, Kim DS (eds) Proceedings of the 19th International Conference on Soil Mechanics and Geotechnical Engineering, ISSMGE, Seoul, vol 2, pp 719–722

[9] Cudny M, Staszewska K (2021) A hyperelastic model for soils with stress-induced and inherent anisotropy. Acta Geotchnica 16:1983–2001, DOI 10.1007/s11440-021-01159-z

[10] Cudny M, Truty A (2020) Refinement of the Hardening Soil model within the small strain range. Acta Geotchnica 15(8):2031–2051, DOI 10.1007/s11440-020-00945-5

[11] Ellison KC, Soga K, Simpson B (2012) A strain space soil model with evolving stiffness anisotropy. Géotechnique 62(7):627–641, DOI 10.1680/geot.10.P.095

[12] Franzius J, Potts D, Burland JB (2005) The influence of soil anisotropy and K_0 on ground surface movements resulting from tunnel excavation. Géotechnique 55(3):189–199, DOI 10.1680/geot.2005.55.3.189

[13] Gasparre A (2005) Advanced laboratory characterisation of London Clay. PhD thesis, Imperial College, London

[14] Gasparre A, Nishimura S, Minh NA, Coop MR, Jardine RJ (2007) The stiffness of natural London Clay. Géotechnique 57(1):33–47, DOI 10.1680/geot.2007.57.1.33

[15] González NA, Rouainia M, Arroyo M, Gens A (2012) Analysis of tunnel excavation in London Clay incorporating soil structure. Géotechnique 62(12):1095–10109, DOI 10.1680/geot.11.P.030

[16] Grammatikopoulou A, Zdravković L, Potts DM (2008) The influence of previous stress history and stress path direction on the surface settlement trough induced by tunnelling. Géotechnique 58(4):269–281, DOI 10.1680/geot.2008.58.4.269

[17] Gudehus G, Mašín D (2009) Graphical representation of constitutive equations. Géotechnique 59(2):147–151, DOI 10.1680/geot.2007.00155

[18] Hight DW, Higgins KG (1995) An approach to the prediction of ground movements in engineering practice: Background and application. In: Shibuya M, Miura (eds) Proceedings of the First International Conference on Pre-failure Deformation Characteristics of Geomaterials, Sapporo, vol 2, pp 909–945

[19] Hight DW, Gasparre A, Nishimura S, Minh NA, Jardine RJ, Coop MR (2007) Characteristics of the London Clay from the Terminal 5 site at Heathrow Airport. Géotechnique 57(1):3–18, DOI 10.1680/geot.2007.57.1.3

[20] Jeremić B, Sture S (1997) Implicit integrations in elastoplastic geotechnics. Mechanics of Cohesive-frictional Materials 2(2):165–183, DOI 10.1002/(SICI)1099-1484(199704)2: 2⟨165::AID-CFM31⟩3.0.CO;2-3

[21] Jovičić V, Jurečič N, Vilhar G (2023) Modelling the structure and anisotropy of London Clay using the SA BRICK model. Applied Sciences 13(2):1–26, DOI 10.3390/app13020880

[22] Länsivaara T, Nordal S (1998) A soil model for the overconsolidated region of clays. In: Pande, Pietruszczak (eds) 4th European Conference on Numerical Methods in Geotechnical Engineering, NUMGE98, Springer, Udine, pp 347–356

[23] Lee KM, Rowe RK (1989) Deformations caused by surface loading and tunnelling: the role of elastic anisotropy. Géotechnique 39(1):125–140, DOI 10.1680/geot.1989.39.1.125

[24] Lehane BM, Simpson B (2000) Modelling glacial till under triaxial conditions using a BRICK soil model. Canadian Geotechnical Journal 37(5):1078–1088, DOI 10.1139/t00-032

[25] Matsuoka H, Nakai T (1977) Stress-strain relationship of soil base on the smp, constitutive equations of soils. In: Murayama, Schofield (eds) Proceedings of the 9th International

Conference on Soil Mechanics and Foundation Engineering, Speciality Session, Tokyo, vol 9, pp 153–162

[26] Mašín D, Rott J (2014) Small strain stiffness anisotropy of natural sedimentary clays: review and a model. Acta Geotechnica 9(2):299–312, DOI 10.1007/s11440-013-0271-2

[27] Mitaritonna G, Amorosi A, Cotecchia F (2014) Experimental investigation of the evolution of elastic stiffness anisotropy in a clayey soil. Géotechnique 64(6):463–475, DOI 10.1680/geot.13.P.191

[28] Mróz Z (1967) On the description of anisotropic workhardening. Journal of the Mechanics and Physics of Solids 15(3):163–175, DOI 10.1016/0022-5096(67)90030-0

[29] Ng C, Leung E, Lau C (2004) Inherent anisotropic stiffness of weathered geomaterial and its influence on ground deformations around deep excavations. Canadian Geotechnical Journal 41:12–24, DOI 10.1139/t03-066

[30] Niemunis A, Grandas Tavera C, Wichtmann T (2016) Peak stress obliquity in drained and undrained sands. Simulations with neohypoplasticity. In: Triantafyllidis T (ed) Holistic Simulation of Geotechnical Installation Processes, Numerical and Physical Modelling, Springer, vol 80, pp 85–114

[31] Nishimura S (2005) Laboratory study on anisotropy of natural London Clay. PhD thesis, Imperial College, London

[32] Nyren R (1998) Field measurements above twin tunnels in London Clay. PhD thesis, Imperial College London

[33] Puzrin AM, Burland JR J Band Strandind (2012) Simple approach to predicting ground displacements caused by tunnelling in undrained anisotropic elastic soil. Géotechnique 62(4):341–352, DOI 10.1680/geot.10.P.127

[34] Puzrin AM, Houlsby GT (2001) Strain-based plasticity models for soils and the BRICK model as an example of the hyperplasticity approach. Géotechnique 51(2):169–172, DOI 10.1680/geot.2001.51.2.169

[35] Santos JA, Correia AG (2001) Reference threshold shear strain of soils. its application to obtain a unique strain-dependent shear modulus curve for soil. In: Proceedings of the 15th International Conference on Soil Mechanics and Geotechnical Engineering, Balkema, Istanbul, Turkey, vol 1, pp 267–270

[36] Simpson B (1992) Retaining structures: displacement and design, 32nd Rankine Lecture. Géotechnique 42(4):541–576, DOI 10.1680/geot.1992.42.4.541

[37] Simpson B, O'Riordan NJ, Croft DD (1979) A computer model for the analysis of ground movements in London Clay. Géotechnique 29(2):149–175, DOI 10.1680/geot.1979.29.2.149

[38] Simpson B, Atkinson JH, Jovičić V (1996) The influence of anisotropy on calculations of ground settlements above tunnels. In: Mair, Taylor (eds) Geotechnical Aspects of Underground Construction in Soft Ground, Balkema: Rotterdam, pp 591–594

[39] Sivakumar V, Doran IG, Graham J, Johnson A (2001) The effect of anisotropic elasticity on the yielding characteristics of overconsolidated natural clay. Canadian Geotechnical Journal 38:125–137, DOI 10.1139/t00-074

[40] Standing JR, Burland JB (2006) Unexpected tunnelling volume losses in the Westminster area, London. Géotechnique 56(1):11–26, DOI 10.1680/geot.2006.56.1.11

[41] Standing JR, Nyren RJ, Burland JB (1996) The measurement of ground movements due to tunnelling at two control sites along the Jubilee Line Extension. In: Mair, Taylor (eds) Geotechnical Aspects of Underground Construction in Soft Ground, Balkema: Rotterdam, pp 751–756

[42] Venda Oliveira PJ, Araújo Santos LM, Almeida e Sousa JNV, Lemos LJL (2021) Effect of initial stiffness on the behaviour of two geotechnical structures: An embankment and a tunnel. Computers and Geotechnics 136, DOI 10.1016/j.compgeo.2021.104181

[43] Vermeer PA (1985) A five constant model unifying well established concepts. In: Gudehus D, Vardoulakis (eds) Constitutive Relations of soils, Balkema, Rotterdam, pp 175–197

[44] Wongsaroj J, Soga K, Mair RJ (2007) Modelling of long-term ground response to tunnelling under St James's Park, London. Géotechnique 57(1):75–90, DOI 10.1680/geot.2007.57.1.75

[45] Yeow HC, R CM (2017) The constitutive modelling of London Clay. Proceedings of the
     Institution of Civil Engineers - Geotechnical Engineering 170(1):3–15, DOI 10.1680/jgeen.
     15.00146

[46] Zwanenburg C (2005) The influence of anisotropy on the consolidation behaviour of peat.
     PhD thesis, Delft University of Technology

[47] Zymis DM, Chatzigiannelis I, Whittle AJ (2015) Effect of anisotropy in ground movements
     caused by tunnelling. Géotechnique 63(13):1083–1102, DOI 10.1680/geot.12.P.056